Bayesian Inversion of Time-Lapse Seismic AVO Data for Multimodal Reservoir Properties

Ole Bernhard Forberg, Dario Grana, and Henning Omre

***Abstract*— We consider time-lapse seismic amplitude versus offset (AVO) inversion for the reservoir properties porosity and water saturation, with a focus on monitoring the evolution of water saturation in a dynamic setting of ongoing production. We operate in a Bayesian framework based on the integration of seismic AVO modeling and rock physics relations. One major challenge in the inversion of seismic data for reservoir properties is the multimodality of these properties. Fluid saturation is generally bimodal due to the gravity effect, and often distinctly so, with abrupt spatial mode transitions. The novelty of the proposed approach is the assumption of a selection Gaussian random field (S-GRF) for the prior spatial model of porosity and water saturation, which can represent the multimodal characteristics of these reservoir properties. The likelihood model is Gauss-linear and based on linearized seismic and rock physics models, which entails that the associated posterior model is also an S-GRF, with analytically assessable parameters. Hence, the posterior model is capable of representing multimodality and abrupt spatial mode transitions. Two realistic case studies are considered; the production of an oil reservoir in the North Sea, and the injection of CO_2 into a subsurface potential CO_2 storage unit. Focus is on the movement of the oil–water-contacts along a vertical profile in the first case, and on the expansion of the CO_2 region in a cross section in the other, both of which can be inferred from the changes in the water saturations. The results are considered to be very encouraging and the proposed statistical formulation appears to be particularly well suited for fluid monitoring problems of the described type.**

***Index Terms*— Geophysics, geophysical measurements, inverse problems, seismic measurements, statistics.**

I. Introduction

DYNAMIC changes in subsurface reservoirs, such as variations in fluid saturations in porous rocks, are often monitored using time-lapse seismic data. If the saturations in the pore spaces change, the velocity of the seismic waves also changes, causing a different seismic response. Time-lapse seismic data can be used to monitor changes in hydrocarbon reservoirs, when water replaces hydrocarbon during production [1], or in carbon dioxide sequestration in deep saline aquifers where CO_2 replaces water [2]. If water replaces hydrocarbon, the velocity of the seismic waves generally increases, whereas if CO_2 replaces water, the velocity generally decreases. According to rock physics studies, the change in seismic velocities and responses increase with increasing pore volume [3].

Geophysics theory, based on wave propagation [4] and rock physics models [3], allow predicting the seismic response of a porous rock with a given porosity and saturation. However, in practice, the rock properties are unknown and the seismic responses are the observable data. Therefore, the prediction of reservoir properties from time-lapse seismic data can be formulated as an inverse problem [5]. Seismic amplitude versus offset (AVO) inversion for static reservoir characterization and time-lapse monitoring is one of the most popular techniques in reservoir geophysics [6]. The forward seismic model can be approximated using linearized approximations or can be based on the full waveform approach. Similarly, the rock physics model can be approximated using multilinear regressions or can be based on poroelasticity theory. Different rock properties and data types can be adopted: data can contain pre-stack or post-stack seismic data and rock properties can include petrophysical properties, such as porosity and saturations, or elastic properties, such as velocities and impedances. Deterministic and probabilistic approaches can be proposed for the solution of the inverse problem [6].

When repeated seismic surveys are available, the inverse problem can be solved simultaneously or as a set of multiple inversions at different time steps. Several methods have been proposed to solve the time-lapse inverse problem, as in [1] and [7]. Here, we focus on the methods incorporating rock physics models for the prediction of rock and fluid properties, as in [8] and [9]. The rock physics model proposed in [8] is based on the approximation of the changes in the reflectivity coefficients as a linear and quadratic function of the changes in saturation and pressure. This model has been used in different applications including hydrocarbon reservoir and CO_2 monitoring studies, as in [10]–[12] and has later been improved using more accurate approximations in [13]–[15]. Alternatively, approximated rock physics models can be combined with the linearized seismic AVO formulation in Bayesian approaches as in [16]–[18]. Bayesian methods have also been combined with optimization approaches for seismic inversion, as in [19]–[21].

Generally, in geophysical inverse problems, the forward model is assumed to be known. We approximate the seismic forward model as a convolution of a wavelet and a linearized approximation [4] of the Zoeppritz equations [22]. This model

Manuscript received June 3, 2020; revised October 23, 2020; accepted November 18, 2020. This work was supported by the Uncertainty in Reservoir Evaluation (URE) research project at the Norwegian University of Science and Technology (NTNU). *(Corresponding author: Ole Bernhard Forberg.)*

Ole Bernhard Forberg and Henning Omre are with the Department of Mathematical Sciences, Norwegian University of Science and Technology, 7491 Trondheim, Norway (e-mail: ole.b.forberg@ntnu.no).

Dario Grana is with the Department of Geology and Geophysics, University of Wyoming, Laramie, WY 82071 USA.

Color versions of one or more figures in this article are available at https://doi.org/10.1109/TGRS.2020.3046102.

Digital Object Identifier 10.1109/TGRS.2020.3046102

predicts the seismic response based on the values of the elastic properties: P-wave velocity, S-wave velocity, and density or P-impedance, S-impedance, and density, as in [23]. The proposed relation is a first-order representation of the wave propagation model [4]. Furthermore, the rock physics model is a multilinear regression in the logarithmic domain of the elastic properties. This model predicts the elastic response, in the logarithmic domain, based on the values of the reservoir properties porosity and fluid saturations [24]. The resulting equation is a first-order of the full rock physics model [3].

In this study, we focus on the inversion of time-lapse seismic AVO data for porosity and saturation using a probabilistic approach. We operate in a Bayesian framework, see [5], to assess the posterior probability distribution of porosity and saturation conditioned on the measured seismic data. This entails that the solution to the inverse problem is in the form of a probability distribution, termed the posterior model, which is proportional to the product of the prior model and the likelihood model. The likelihood model is a probabilistic representation of the geophysical model including seismic and rock physics relations. In Bayesian approaches for geophysical inverse problems, the likelihood model is generally assumed to be linear with Gaussian errors that are independent of the model ([25] and [5]). The prior model of the reservoir properties represents the prior knowledge about them. If the prior model of the reservoir properties is Gaussian, under the above-mentioned assumptions of the likelihood model, the posterior model is also Gaussian, and the solution can be analytically evaluated. Due to the large dimensionality of the gridded geophysical data, an analytical solution is desirable [26].

However, the reservoir properties are generally not well represented by a Gaussian prior model because porosity and fluid saturations represent volumetric fractions, hence bounded properties, and their spatial histograms are often multimodal within the domain of physically admissible values. For a general prior model, the posterior model is not necessarily Gaussian and iterative simulation-based methods have to be adopted, such as Markov chain Monte Carlo (McMC) methods [27]. These methods enable the assessment of the posterior distribution by proposing from the prior model and accepting or rejecting the proposal based on the likelihood. However, the convergence can be relatively slow for a large dimensional geophysical data set, if a spatial correlation model is included [28].

The multimodal appearance of reservoir properties is usually caused by the presence of underlying litho-fluid classes in the subsurface. Sandstone generally have larger porosity than shale. Hence, in a sequence of sand and shale, porosity is generally bimodal. Similarly, within the reservoir, porous rocks can be saturated with different fluids; for example, water and hydrocarbon or water and CO_2, leading to bimodal histograms for fluid saturations. These multimodalities can be modeled using Gaussian mixture models ([24], [29], [30] and [31]). The solution of the inverse problem based on spatial Gaussian mixture models usually relies on computationally demanding McMC algorithms. Inversion methods including hidden Markov models have also been proposed to integrate a spatial model in the solution for the classification of facies from geophysical data ([32], [33] and [34]).

We propose an alternative prior model for multimodal reservoir properties based on selection Gaussian random fields (S-GRFs), based on results in [35] and [31]. The selection Gaussian model can represent multimodal and skewed variables while preserving the analytical advantages of the Gaussian case; namely if the prior model is selection Gaussian and the likelihood model is linear and Gaussian, then the posterior model is also selection Gaussian [31] with analytically assessable parameters.

The methodology is validated using two different applications based on real data sets. The first application is based on the well logs data from a vertical well in a hydrocarbon reservoir in the North Sea. Synthetic seismic data are generated before and after 10 years of production assuming depletion and water flooding. The second application is based on a 2-D cross section of a reservoir model of a deep saline aquifer used for CO_2 sequestration. A fluid flow model is applied to simulate the injection of CO_2 for 110 years. Synthetic seismic data are generated after 10 and 100 years of production. In both applications, we compute the posterior distribution of porosity and water saturation.

II. Definitions and Notation

The reservoir volume of interest is discretized into a regular grid $\mathcal{G}_r$, consisting of n_r points. At a given time the n_r-dimensional vectors $\boldsymbol{\phi}$ and $\mathbf{s}_w$ contain the porosities and water saturations on all of $\mathcal{G}_r$. In the time-lapse setting, we consider the reservoir volume at two different points in time. We assume the porosities to be temporally constant and the water saturations to be dynamic; hence, a superscript t is introduced for the water saturations to indicate the time of evaluation, $\mathbf{s}_w^t$, $t = 0, 1$. The porosities and water saturations jointly constitute the reservoir properties $\mathbf{r}$ on the entire reservoir grid, i.e., $\mathbf{r} = [\boldsymbol{\phi}, \mathbf{s}_w^0, \mathbf{s}_w^1]$, with $[\cdot, \ldots, \cdot]$ the concatenation of its arguments. The seismic AVO data associated with the reservoir properties on $\mathcal{G}_r$ is collected on the grid $\mathcal{G}_d$, consisting of n_d points, and is acquired at n_θ different offset angles and at the two time points $t = 0, 1$. The $2n_\theta n_d$-dimensional vector $\mathbf{d}$ contains the time-lapse seismic AVO data on $\mathcal{G}_d$. The three n_r-dimensional vectors $\mathbf{z}_p$, $\mathbf{z}_s$, and $\boldsymbol{\rho}$ represent the elastic rock properties P-impedance, S-impedance, and density on all of $\mathcal{G}_r$, respectively. These properties are represented in the logarithmic form at both time points in the $6n_r$-dimensional vector $\mathbf{m}$. All vectors defined above are defined to be column vectors, and unless otherwise stated, so are subsequently defined vectors.

The function $p(\cdot)$ is a probability density function (pdf) of its argument. An n_x-dimensional random vector $\mathbf{x}$ with expected value $\boldsymbol{\mu}_x$ and covariance matrix $\boldsymbol{\Sigma}_x$ is Gaussian if its pdf is of the form

$$p(\mathbf{x}) = (2\pi)^{-\frac{n_x}{2}} |\boldsymbol{\Sigma}_x|^{-\frac{1}{2}} \exp\left\{ -\frac{1}{2} \left(\mathbf{x} - \boldsymbol{\mu}_x\right)^T \boldsymbol{\Sigma}_x^{-1} \left(\mathbf{x} - \boldsymbol{\mu}_x\right) \right\} \quad (1)$$

where the superscript T indicates the transpose. We denote this pdf by $\varphi_{n_x}(\mathbf{x}; \boldsymbol{\mu}_x, \boldsymbol{\Sigma}_x)$. The probability that $\mathbf{x}$ belongs to

a subset $\mathbf{Q}$ of the n_x-dimensional space of real numbers is specified by

$$\text{Prob}(\mathbf{x} \in \mathbf{Q}) = \int_{\mathbb{R}^{n_x}} I(\mathbf{x} \in \mathbf{Q}) \varphi_{n_x}\left(\mathbf{x}; \boldsymbol{\mu}_x, \boldsymbol{\Sigma}_x\right) \, \mathrm{d}\mathbf{x} \tag{2}$$

and we denote this Gaussian subset probability by $\Phi_{n_x}(\mathbf{Q}; \boldsymbol{\mu}_x, \boldsymbol{\Sigma}_x)$. The function $I(\cdot)$ is the indicator function, being equal to 1 when the argument is true and equal to 0 otherwise.

An n_y-dimensional random vector $\mathbf{y}$ is selection Gaussian with associated Gaussian n_y-dimensional basis variable $\tilde{\mathbf{y}}$ and n_{v_y}-dimensional auxiliary variable $\boldsymbol{v}_y$, and selection set $\mathcal{A}$, see [36] for details, if its pdf is of the form demonstrated in [35]

$$\begin{aligned} p(\mathbf{y}) &= p\left(\tilde{\mathbf{y}} | \boldsymbol{v}_y \in \mathcal{A}\right) = \frac{\text{Prob}(\boldsymbol{v}_y \in \mathcal{A} | \tilde{\mathbf{y}}) p(\tilde{\mathbf{y}})}{\text{Prob}(\boldsymbol{v}_y \in \mathcal{A})} \\ &= \frac{\Phi_{n_v}\left(\mathcal{A}; \boldsymbol{\mu}_{v_y|\tilde{\mathbf{y}}}, \boldsymbol{\Sigma}_{v_y|\tilde{\mathbf{y}}}\right) \varphi_{n_y}\left(\tilde{\mathbf{y}}; \boldsymbol{\mu}_{\tilde{\mathbf{y}}}, \boldsymbol{\Sigma}_{\tilde{\mathbf{y}}}\right)}{\Phi_{n_v}\left(\mathcal{A}; \boldsymbol{\mu}_{v_y}, \boldsymbol{\Sigma}_{v_y}\right)}. \end{aligned} \tag{3}$$

This pdf is fully specified by the parameters $\Theta^{SG} = (\boldsymbol{\mu}_{\tilde{\mathbf{y}}}, \boldsymbol{\mu}_{v_y}, \boldsymbol{\Sigma}_{\tilde{\mathbf{y}}}, \boldsymbol{\Sigma}_{v_y}, \boldsymbol{\Gamma}_{\tilde{\mathbf{y}}v_y}, \mathcal{A})$, where $\boldsymbol{\Gamma}_{\tilde{\mathbf{y}}v_y}$ contains the covariances between $\tilde{\mathbf{y}}$ and $\boldsymbol{v}_y$. From the listed parameters the conditional parameters can be computed by standard Gaussian conditioning formulas

$$\begin{aligned} \boldsymbol{\mu}_{v_y|\tilde{\mathbf{y}}} &= \boldsymbol{\mu}_{v_y} + \boldsymbol{\Gamma}_{\tilde{\mathbf{y}}v_y} \boldsymbol{\Sigma}_{\tilde{\mathbf{y}}}^{-1} \left(\mathbf{y} - \boldsymbol{\mu}_{\tilde{\mathbf{y}}}\right) \\ \boldsymbol{\Sigma}_{v_y|\tilde{\mathbf{y}}} &= \boldsymbol{\Sigma}_{v_y} - \boldsymbol{\Gamma}_{\tilde{\mathbf{y}}v_y} \boldsymbol{\Sigma}_{\tilde{\mathbf{y}}}^{-1} \boldsymbol{\Gamma}_{\tilde{\mathbf{y}}v_y}^T. \end{aligned} \tag{4}$$

A random vector is said to be a discretized random field (RF) if each of its elements is associated with a grid location in a spatial domain. The Gaussian random vector $\mathbf{x}$ is a Gaussian random field (GRF) if $\mathbf{x}$ is an RF. Similarly, the selection Gaussian random vector $\mathbf{y}$ is an S-GRF if $\mathbf{y}$ is an RF.

Lastly, $\mathbf{i}_n$ denotes the n-dimensional vector of ones, and the $(n \times n)$ matrix $\mathbf{I}_n$ is the identity matrix with n rows and n columns. The $(n_1 \times n_2)$ matrix of zeroes is denoted $\mathbf{0}_{n_1 \times n_2}$.

III. Methodology

The aim of the study is to predict the reservoir properties $\mathbf{r}$ from the time-lapse seismic AVO data $\mathbf{d}$. In a Bayesian framework the solution is given by the posterior pdf $p(\mathbf{r}|\mathbf{d})$, and this conditional pdf is defined by Bayes' rule

$$p(\mathbf{r}|\mathbf{d}) = \frac{p(\mathbf{d}|\mathbf{r}) p(\mathbf{r})}{p(\mathbf{d})} \propto p(\mathbf{d}|\mathbf{r}) p(\mathbf{r}) \tag{5}$$

with $p(\mathbf{d}|\mathbf{r})$ being the likelihood model and $p(\mathbf{r})$ the prior model, which both have to be specified. The normalizing constant $[p(\mathbf{d})]^{-1}$ is usually very challenging to compute, but for certain combinations of likelihood and prior models it can be analytically assessed. The current study relies on models of the latter type.

A. Likelihood Model

The likelihood model describes the origin of the seismic responses from the reservoir properties and is decomposed into

$$p(\mathbf{d}|\mathbf{r}) = \int p(\mathbf{d}|\mathbf{m}, \mathbf{r}) p(\mathbf{m}|\mathbf{r}) \, \mathrm{d}\mathbf{m} = \int p(\mathbf{d}|\mathbf{m}) p(\mathbf{m}|\mathbf{r}) \, \mathrm{d}\mathbf{m} \tag{6}$$

with the last equality a result of the elastic properties $\mathbf{m}$ being canonical variables of the wave equation. Hence, the likelihood model consists of two parts; the seismic likelihood model $p(\mathbf{d}|\mathbf{m})$ and the rock physics model $p(\mathbf{m}|\mathbf{r})$.

The seismic likelihood model relates the elastic properties to the seismic responses and is based on a convolution of the linear Aki and Richards [4] approximation to the Zoeppritz equations. The model is linear and Gaussian (Gauss-linear) and takes the form $[\mathbf{d}|\mathbf{m}] = \mathbf{WADm} + \mathbf{e}_{d|m}$, see [23]. Here, the $(2n_\theta n_d \times 2n_\theta n_r)$ matrix $\mathbf{W}$ is a convolution operator containing discretizations of the seismic wavelet at both time points

$$\mathbf{W} = \begin{bmatrix} \mathbf{W}^0 & \mathbf{0}_{n_\theta n_d \times n_\theta n_r} \\ \mathbf{0}_{n_\theta n_d \times n_\theta n_r} & \mathbf{W}^1 \end{bmatrix} \tag{7}$$

with $(n_\theta n_d \times n_\theta n_r)$ matrices $\mathbf{W}^0$ and $\mathbf{W}^1$ containing the discretized seismic wavelet at times $t = 0, 1$, respectively.

The $(2n_\theta n_r \times 6n_r)$ matrix $\mathbf{A}$ and $(6n_r \times 6n_r)$ matrix $\mathbf{D}$ emerge from the Aki and Richards approximation. Here, $\mathbf{A}$ contains the impedance adapted angle dependent reflection coefficients, see [37], at both time points

$$\mathbf{A} = \begin{bmatrix} \mathbf{A}^0 & \mathbf{0}_{n_\theta n_r \times 3n_r} \\ \mathbf{0}_{n_\theta n_r \times 3n_r} & \mathbf{A}^1 \end{bmatrix} \tag{8}$$

with $(n_\theta n_r \times 3n_r)$ matrices $\mathbf{A}^0$ and $\mathbf{A}^1$ corresponding to times $t = 0, 1$, respectively. The matrix $\mathbf{D}$ is a contrast operator. Error associated with the seismic likelihood model is contained in the $2n_\theta n_d$-dimensional vector $\mathbf{e}_{d|m}$, which encompasses both model error and observation error. We assume $\mathbf{e}_{d|m}$ to be Gaussian with expectation zero and $(2n_\theta n_d \times 2n_\theta n_d)$ covariance matrix $\boldsymbol{\Sigma}_{d|m} = \mathbf{W}\sigma_{c|m}^2 \mathbf{I}_{2n_\theta n_r} \mathbf{W}^T + \sigma_{d|c}^2 \mathbf{I}_{2n_\theta n_d}$, where $\sigma_{c|m}^2$ is the variance associated with model error resulting from the Aki and Richards approximation and $\sigma_{d|c}^2$ is the variance associated with observation error. Note that the model error is wavelet convolved in this expression, hence $\mathbf{e}_{d|m}$ contains colored noise. The seismic likelihood model will then be

$$p(\mathbf{d}|\mathbf{m}) = \varphi_{2n_\theta n_d}\left(\mathbf{d}; \mathbf{WADm}, \boldsymbol{\Sigma}_{d|m}\right). \tag{9}$$

Inspired by the study [8], we formulate a linear rock physics model that in line with previous studies [36] is in the form of a multiple linear regression. The model is Gauss-linear and relates the reservoir properties to the elastic properties, $[\mathbf{m}|\mathbf{r}] = \mathbf{Br} + \mathbf{e}_{m|r}$. Here, the $(6n_r \times 3n_r)$ matrix $\mathbf{B}$ contains the regression coefficients from a multiple linear regression of the logarithmic elastic properties on the porosities and water saturations, $\mathbf{B} = [\mathbf{B}^0, \mathbf{B}^1]$, with $(3n_r \times 3n_r)$ matrices $\mathbf{B}^0$ and $\mathbf{B}^1$ containing the regression coefficients at times $t = 0, 1$, respectively. The $6n_r$-dimensional vector $\mathbf{e}_{m|r}$ contains the error resulting from the linear rock physics model. We assume it to be Gaussian with expectation zero and $(6n_r \times 6n_r)$ covariance matrix $\boldsymbol{\Sigma}_{m|r}$ containing the variances associated with the regressions of the logarithmic elastic properties on the porosities and water saturations on the diagonal, while the off-diagonal elements are the covariances between them. Hence, the rock physics model is

$$p(\mathbf{m}|\mathbf{r}) = \varphi_{6n_r}\left(\mathbf{m}; \mathbf{Br}, \boldsymbol{\Sigma}_{m|r}\right). \tag{10}$$

The likelihood model, which relates $\mathbf{d}$ to $\mathbf{r}$, is the sequential application of the rock physics model and the seismic

likelihood model, and takes the form $[\mathbf{d}|\mathbf{r}] = \mathbf{G}\mathbf{r} + \mathbf{e}_{d|r}$, where the $(2n_\theta n_d \times 3n_r)$ matrix $\mathbf{G} = \mathbf{WADB}$ is the forward operator. Furthermore, the $2n_\theta n_d$-dimensional vector $\mathbf{e}_{d|r} = \mathbf{WADe}_{m|r} + \mathbf{e}_{d|m}$ is an error vector assumed to be Gaussian with expectation zero and $(2n_\theta n_d \times 2n_\theta n_d)$ covariance matrix $\mathbf{\Sigma}_{d|r} = \mathbf{WAD}\mathbf{\Sigma}_{m|r}(\mathbf{WAD})^T + \mathbf{\Sigma}_{d|m}$. Hence, the likelihood model is Gauss-linear

$$p(\mathbf{d}|\mathbf{r}) = \varphi_{2n_\theta n_d}\big(\mathbf{d};\, \mathbf{WADBr},\, \mathbf{\Sigma}_{d|r}\big). \tag{11}$$

In a Bayesian framework, Gauss-linearity of the likelihood model is advantageous for several parametric prior models that are conjugate with respect to this type of likelihood model. The posterior model is then on the same form as the prior model, but with different model parameters. Since the likelihood model is jointly defined for the seismic data at both time points, time-lapse inversion can be done simultaneously.

The signal-to-noise ratio (SNR) is a commonly used noise measure for seismic data and is defined as the average variance of the signal divided by the average variance of the noise

$$\text{SNR} = \frac{\text{trace}(\text{Var}(\mathbf{Gr}))}{\text{trace}(\text{Var}(\mathbf{d}|\mathbf{r}))} = \frac{\text{trace}\big(\mathbf{G}\mathbf{\Sigma}_r\mathbf{G}^T\big)}{\text{trace}\big(\mathbf{\Sigma}_{d|r}\big)} \tag{12}$$

where trace$(\cdot)$ returns the sum of the diagonal elements of the argument. Note that the covariance matrix $\mathbf{\Sigma}_r$ is defined by the prior model $p(\mathbf{r})$.

B. Prior Model

The prior model $p(\mathbf{r})$ should reflect our prior knowledge and understanding of the reservoir properties we want to predict. We choose a selection Gaussian prior model due to its flexibility and support for nonsymmetric and multimodal characteristics, see [36]. We construct the model by using the decomposition

$$p(\tilde{\mathbf{r}}, \boldsymbol{\nu}) = p(\boldsymbol{\nu}|\tilde{\mathbf{r}})p(\tilde{\mathbf{r}}) \tag{13}$$

where the $3n_r$-dimensional vector $\tilde{\mathbf{r}} = [\tilde{\mathbf{r}}_1, \tilde{\mathbf{r}}_2, \tilde{\mathbf{r}}_3] = [\tilde{\boldsymbol{\phi}}, \tilde{\mathbf{s}}^0_w, \tilde{\mathbf{s}}^1_w]$ is the basis variable for $\mathbf{r}$, and the $3n_r$-dimensional vector $\boldsymbol{\nu} = [\boldsymbol{\nu}_1, \boldsymbol{\nu}_2, \boldsymbol{\nu}_3]$ is the auxiliary variable.

The basis variable is assumed to be a stationary GRF on $\mathcal{G}_r$

$$p(\tilde{\mathbf{r}}) = \varphi_{3n_r}(\tilde{\mathbf{r}};\, \boldsymbol{\mu}_{\tilde{r}},\, \mathbf{\Sigma}_{\tilde{r}}) \tag{14}$$

with

$$\boldsymbol{\mu}_{\tilde{r}} = \begin{bmatrix} \mu_{\tilde{\phi}}\mathbf{i}_{n_r} \\ \mu_{\tilde{s}^0_w}\mathbf{i}_{n_r} \\ \mu_{\tilde{s}^1_w}\mathbf{i}_{n_r} \end{bmatrix}$$

$$\mathbf{\Sigma}_{\tilde{r}} = \begin{bmatrix} \sigma^2_{\tilde{\phi}}\mathbf{\Omega} & \lambda_1\sigma_{\tilde{\phi}}\sigma_{\tilde{s}^0_w}\mathbf{\Omega} & \lambda_2\sigma_{\tilde{\phi}}\sigma_{\tilde{s}^1_w}\mathbf{\Omega} \\ \lambda_1\sigma_{\tilde{\phi}}\sigma_{\tilde{s}^0_w}\mathbf{\Omega} & \sigma^2_{\tilde{s}^0_w}\mathbf{\Omega} & \lambda_3\sigma_{\tilde{s}^0_w}\sigma_{\tilde{s}^1_w}\mathbf{\Omega} \\ \lambda_2\sigma_{\tilde{\phi}}\sigma_{\tilde{s}^1_w}\mathbf{\Omega} & \lambda_3\sigma_{\tilde{s}^0_w}\sigma_{\tilde{s}^1_w}\mathbf{\Omega} & \sigma^2_{\tilde{s}^1_w}\mathbf{\Omega} \end{bmatrix}. \tag{15}$$

Here, $\mu_{\tilde{\phi}}$, $\mu_{\tilde{s}^0_w}$, and $\mu_{\tilde{s}^1_w}$ are the expectation levels and $\sigma^2_{\tilde{\phi}}$, $\sigma^2_{\tilde{s}^0_w}$, and $\sigma^2_{\tilde{s}^1_w}$ the variance levels of $\tilde{\boldsymbol{\phi}}$, $\tilde{\mathbf{s}}^0_w$, and $\tilde{\mathbf{s}}^1_w$, respectively. Furthermore, the $(n_r \times n_r)$ correlation matrix $\mathbf{\Omega}$ contains the spatial correlations, and is defined through the exponential correlation function $\rho_r(\tau;\alpha_r) = \exp\{-\tau/\alpha_r\}$. Here, $\tau > 0$ is the distance between grid locations and $\alpha_r > 0$ is the range parameter. The correlations between $\tilde{\phi}_i$ and $\tilde{s}^0_{w,i}$, between $\tilde{\phi}_i$ and $\tilde{s}^1_{w,i}$, and between $\tilde{s}^0_{w,i}$ and $\tilde{s}^1_{w,i}$ are λ_1, λ_2, and λ_3 for all grid points $i = 1, \ldots, n_r$ due to stationarity, respectively.

The auxiliary variable $\boldsymbol{\nu}$ is Gauss-linearly and conditionally independently related to the basis variable

$$\begin{aligned} p(\boldsymbol{\nu}|\tilde{\mathbf{r}}) &= p(\boldsymbol{\nu}_1|\tilde{\mathbf{r}}_1)p(\boldsymbol{\nu}_2|\tilde{\mathbf{r}}_2)p(\boldsymbol{\nu}_3|\tilde{\mathbf{r}}_3) \\ &= \prod_{k=1}^{3} \varphi_{n_r}\big(\boldsymbol{\nu}_k;\, \boldsymbol{\mu}_{\nu_k|\tilde{r}_k},\, \big(1-\gamma_k^2\big)\mathbf{I}_{n_r}\big) \\ &= \prod_{k=1}^{3}\left(\prod_{i=1}^{n_r} \varphi_1\big(\nu_{k,i};\, \mu_{\nu_{k,i}|\tilde{r}_k},\, \big(1-\gamma_k^2\big)\big)\right). \end{aligned} \tag{16}$$

The conditional means are $\boldsymbol{\mu}_{\nu_k|\tilde{r}_k} = 0\mathbf{i}_{n_r} + \mathbf{\Gamma}_{\nu_k\tilde{r}_k}\mathbf{\Sigma}^{-1}_{\tilde{r}_k}(\tilde{\boldsymbol{r}}_k - \mu_{\tilde{r}_k}\mathbf{i}_{n_r})$, with $\mathbf{\Gamma}_{\nu_k\tilde{r}_k} = \gamma_k\sigma_{\tilde{r}_k}\mathbf{\Omega}$ being the cross-covariance matrix between $\tilde{\mathbf{r}}_k$ and $\boldsymbol{\nu}_k$, for $k = 1, 2, 3$. Moreover, γ_k is the correlation between $\tilde{r}_{k,i}$ and $\nu_{k,i}$. Associated with each auxiliary variable is the n_r-dimensional selection set $\mathbf{A}_k = A_k^{n_r}$, with A_k a subset of the real numbers. These selection sets are contained in $\mathbf{A}$.

Since $p(\tilde{\mathbf{r}})$ is Gaussian and $p(\boldsymbol{\nu}|\tilde{\mathbf{r}})$ is Gauss-linear, the joint pdf $p(\tilde{\mathbf{r}}, \boldsymbol{\nu})$ is Gaussian

$$p(\tilde{\mathbf{r}}, \boldsymbol{\nu}) = \varphi_{6n_r}\left(\begin{bmatrix}\tilde{\mathbf{r}} \\ \boldsymbol{\nu}\end{bmatrix}; \begin{bmatrix}\boldsymbol{\mu}_{\tilde{r}} \\ 0\mathbf{i}_{3n_r}\end{bmatrix}, \begin{bmatrix}\mathbf{\Sigma}_{\tilde{r}} & \mathbf{\Gamma}_{\tilde{r}\nu} \\ \mathbf{\Gamma}_{\nu\tilde{r}} & \mathbf{\Sigma}_{\nu}\end{bmatrix}\right). \tag{17}$$

The $(3n_r \times 3n_r)$ matrix $\mathbf{\Gamma}_{\tilde{r}\nu} = \mathbf{\Gamma}^T_{\nu\tilde{r}}$ contains the cross-covariance between $\tilde{\mathbf{r}}$ and $\boldsymbol{\nu}$

$$\mathbf{\Gamma}_{\tilde{r}\nu} = \begin{bmatrix} \gamma_1\sigma_{\tilde{\phi}}\mathbf{\Omega} & \lambda_1\gamma_2\sigma_{\tilde{\phi}}\mathbf{\Omega} & \lambda_2\gamma_3\sigma_{\tilde{\phi}}\mathbf{\Omega} \\ \lambda_1\gamma_1\sigma_{\tilde{s}^0_w}\mathbf{\Omega} & \gamma_2\sigma_{\tilde{s}^0_w}\mathbf{\Omega} & \lambda_3\gamma_3\sigma_{\tilde{s}^0_w}\mathbf{\Omega} \\ \lambda_2\gamma_1\sigma_{\tilde{s}^1_w}\mathbf{\Omega} & \lambda_3\gamma_2\sigma_{\tilde{s}^1_w}\mathbf{\Omega} & \gamma_3\sigma_{\tilde{s}^1_w}\mathbf{\Omega} \end{bmatrix}. \tag{18}$$

Furthermore, the $(3n_r \times 3n_r)$ covariance matrix $\mathbf{\Sigma}_\nu$ associated with $\boldsymbol{\nu}$, is defined as

$$\mathbf{\Sigma}_\nu = \begin{bmatrix} \mathbf{\Sigma}_{\nu_1} & \lambda_1\gamma_1\gamma_2\mathbf{\Omega} & \lambda_2\gamma_1\gamma_3\mathbf{\Omega} \\ \lambda_1\gamma_1\gamma_2\mathbf{\Omega} & \mathbf{\Sigma}_{\nu_2} & \lambda_3\gamma_2\gamma_3\mathbf{\Omega} \\ \lambda_2\gamma_1\gamma_3\mathbf{\Omega} & \lambda_3\gamma_2\gamma_3\mathbf{\Omega} & \mathbf{\Sigma}_{\nu_3} \end{bmatrix} \tag{19}$$

with

$$\mathbf{\Sigma}_{\nu_k} = \gamma_k^2\mathbf{\Omega} + \big(1-\gamma_k^2\big)\mathbf{I}_{n_r}, \quad k = 1, 2, 3. \tag{20}$$

The prior model is a discretized stationary S-GRF with pdf

$$\begin{aligned} p(\mathbf{r}) &= p(\tilde{\mathbf{r}}|\boldsymbol{\nu} \in \mathbf{A}) \\ &= \frac{\prod_{k=1}^{3}\prod_{i=1}^{n_r} \Phi_1\big(A_k;\, \mu_{\nu_{k,i}|\tilde{r}_k},\, \big(1-\gamma_k^2\big)\big)}{\Phi_{3n_r}\big(\mathbf{A};\, 0\mathbf{i}_{3n_r},\, \mathbf{\Sigma}_\nu\big)}\varphi_{3n_r}(\tilde{\mathbf{r}};\, \boldsymbol{\mu}_{\tilde{r}},\, \mathbf{\Sigma}_{\tilde{r}}). \end{aligned} \tag{21}$$

The stationarity of the RF implies that all model parameters, except the correlations, can be inferred from spatial histograms of the reservoir properties. The parameters associated with the marginal prior models $p(r_k)$ are inferred from spatial histograms of the observed or true $\mathbf{r}_k$, while the intervariable correlations λ_k are inferred from scatterplots. The spatial locations associated with the reservoir properties are used to assess the spatial correlation.

The reservoir properties are physically limited to the range [0, 1]. Defining a continuous prior model honoring these limits is challenging, with every solution having its drawbacks. One possibility is transforming the reservoir properties from [0, 1] to the real numbers, e.g., by the logit transformation. However,

this approach may introduce increased multimodality due to steep gradients near the borders of the range [0, 1]. One could also use a truncated prior model, but this may depending on the definition of the predictor, yield erroneous predictions that are difficult to correct. Another possibility is to allow the prior model to support nonphysical values slightly outside [0, 1] and correct for this in the predictor. Since the focus is on the results of the methodology, we choose the latter approach due to its simplicity and effectiveness.

C. Posterior Model

The Gauss-linearity of the likelihood model $p(\mathbf{d}|\mathbf{r})$ induce conjugacy in the prior model defined above; hence, the posterior model is an S-GRF, see [31]. The posterior pdf is

$$\begin{aligned} p(\mathbf{r}|\mathbf{d}) &= p(\tilde{\mathbf{r}}|\boldsymbol{\nu} \in \mathbf{A}, \mathbf{d}) \\ &= \frac{\prod_{k=1}^{3} \Phi_{n_r}\left(\mathbf{A}_k; \boldsymbol{\mu}_{\nu_k|\tilde{r}_k,d}, \boldsymbol{\Sigma}_{\nu_k|\tilde{r}_k,d}\right)}{\Phi_{3n_r}\left(\mathbf{A}; \boldsymbol{\mu}_{\nu|d}, \boldsymbol{\Sigma}_{\nu|d}\right)} \varphi_{3n_r}\left(\tilde{\mathbf{r}}; \boldsymbol{\mu}_{\tilde{r}|d}, \boldsymbol{\Sigma}_{\tilde{r}|d}\right) \end{aligned} \tag{22}$$

and the conditional parameters involved in the model and the McMC algorithm used for assessment can be found in [36].

D. Predictor

We identify the locationwise most probable values of the reservoir properties from the posterior distribution. This, the marginal maximum posterior (MMAP), is defined to be the predictor

$$\hat{\mathbf{r}}_{\text{MMAP}} = \left\{ \underset{r_{k,i}}{\text{argmax}} \left\{ p\left(r_{k,i}|\mathbf{d}\right) \right\}, \quad k = 1, 2, 3, \;\; i = 1, \ldots, n_r \right\}. \tag{23}$$

Furthermore, we use $(1-\alpha) \times 100\%$ highest posterior density (HPD) prediction intervals to accompany the predictions. A HPD prediction interval attains the desired $(1-\alpha) \times 100\%$ coverage by encompassing only the most probable regions that cumulatively integrate to $(1-\alpha) \times 100\%$. These regions need not be connected; hence, a HPD prediction interval may consist of a collection of disjoint regions, thereby reflecting multimodality in the posterior distribution. HPD prediction intervals are therefore natural to use in the S-GRF framework. The coverage level $(1-\alpha) \times 100\%$ is arbitrary and determined by the user. The choice is usually influenced by the application and the form of the posterior distribution. Commonly used coverage levels are 80%, 90%, 95%, and 99%. In a setting of HPD prediction intervals, it is natural to select a coverage level resulting in prediction intervals that reflect the shape of the distribution.

Since the prior model can support nonphysical values, so can the MMAP and HPD prediction interval. Should they exceed [0, 1], they are truncated to the appropriate limits of this range.

IV. 1-D Application: Oil Production

We first validate the seismic inversion methodology using a well log data set from a vertical well in the North Sea, see [37]. The data were measured in a clastic reservoir partially filled by oil and include sonic logs, petrophysical logs, and estimated volumetric curves. The depth interval considered in this study, hereafter referred to as the study interval, contains a sequence of sand and shale interpreted using the gamma ray log. The sand layers have mid-to-high effective porosity computed from the density and neutron porosity log. Two main oil reservoir zones can be identified; one in the middle part and the other in the lower part of the study interval. Oil saturation is calculated from the resistivity log in the clean sand layers using Archie's law. The well logs were measured one year prior to oil production. The production mechanism is water injection through a nearby well and oil extraction from the two layers. Based on fluid flow simulations 10 years ahead, saturation profiles are predicted at the well location, resulting in partial saturations in the two reservoir layers. The measured pre-production well logs and the in-production predicted saturation profile, shown in Fig. 1, are used to generate synthetic time-lapse seismic AVO data at the well location. Note that the in-production water saturation has an increase in highly saturated locations from the bottom-up within both oil reservoirs compared to the pre-production water saturation, which reflects the production mechanism. Uncorrelated Gaussian noise is added to the synthetic data assuming an SNR of 5. The pre-production elastic properties are available from the well logs, while the in-production velocities and density are computed from the porosity and predicted saturation profile by Gassmann's equation. We assume that only the pre-production well logs are known; hence, the likelihood and prior models must be assigned based on these. However, the predicted saturation profile will be used to validate the inversion result. The porosity and water saturation profiles used to generate the synthetic time-lapse seismic data are referred to as the truth.

The study interval has a reservoir grid $\mathcal{G}_r$ consisting of $n_r = 105$ regularly spaced locations, while the seismic grid $\mathcal{G}_d$ consists of $n_d = 104$ locations being a subset of $\mathcal{G}_r$.

The time-lapse seismic AVO data associated with the problem is presented in Fig. 2 and consists of $n_\theta = 3$ angle stacks. The stacking angles are adopted from a seismic processing study in a nearby field. The estimated critical angle is approximately 45°, hence the linearized Zoeppritz equations provide an accurate approximation of the reflection coefficients for all angle stacks used in this study. There is a visible difference in the pre-production and in-production seismic data in the middle part and lower part of the study interval, coinciding with the locations of the two oil reservoir zones.

A. Likelihood Model

Since the seismic data are synthetically generated from the elastic properties, we have full knowledge of the seismic likelihood model $[\mathbf{d}|\mathbf{m}] = \mathbf{WADm} + \mathbf{e}_{d|m}$. Hence, only the rock physics model $[\mathbf{m}|\mathbf{r}] = \mathbf{Br} + \mathbf{e}_{m|r}$ requires parameter estimation, which entails estimation of the parameters involved in the multiple linear regression model, consisting of the coefficients contained in $\mathbf{B}$ and the entries in the covariance matrix $\boldsymbol{\Sigma}_{m|r}$. We apply the same rock physics model in the entire study interval; however, for more complex data sets with

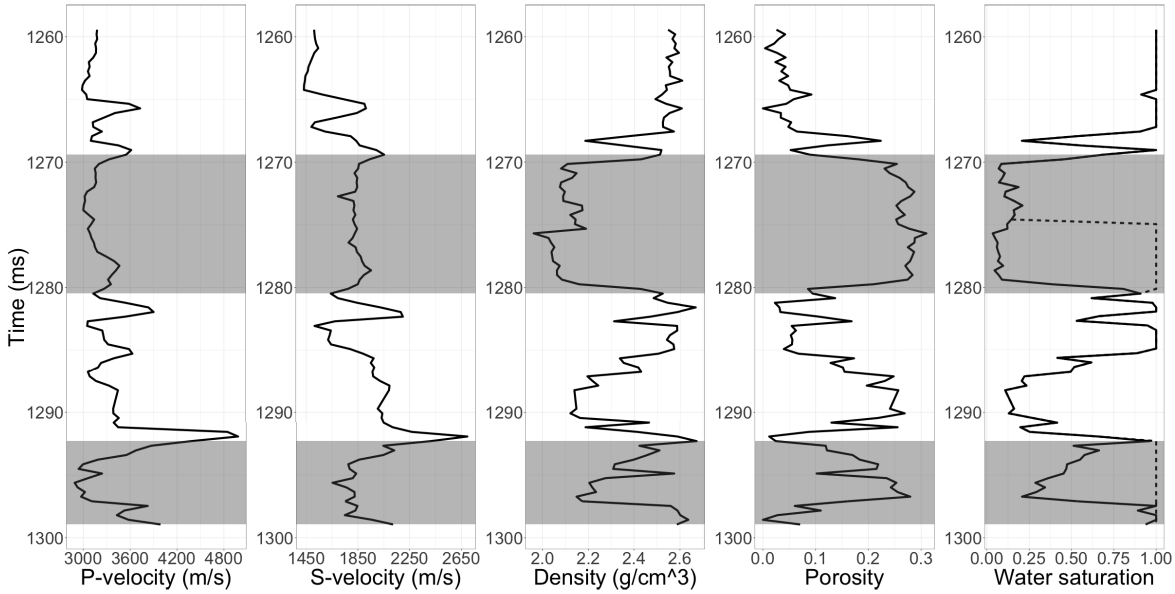

Fig. 1. Well logs. P-velocity, S-velocity, density, porosity, and water saturation displayed column-wise left to right. The two main oil reservoir zones are highlighted by transparent black rectangles. The display of water saturation contains both pre-production (solid line) and in-production (dashed line) water saturations, and the saturations coincide at depths where only a solid line is present.

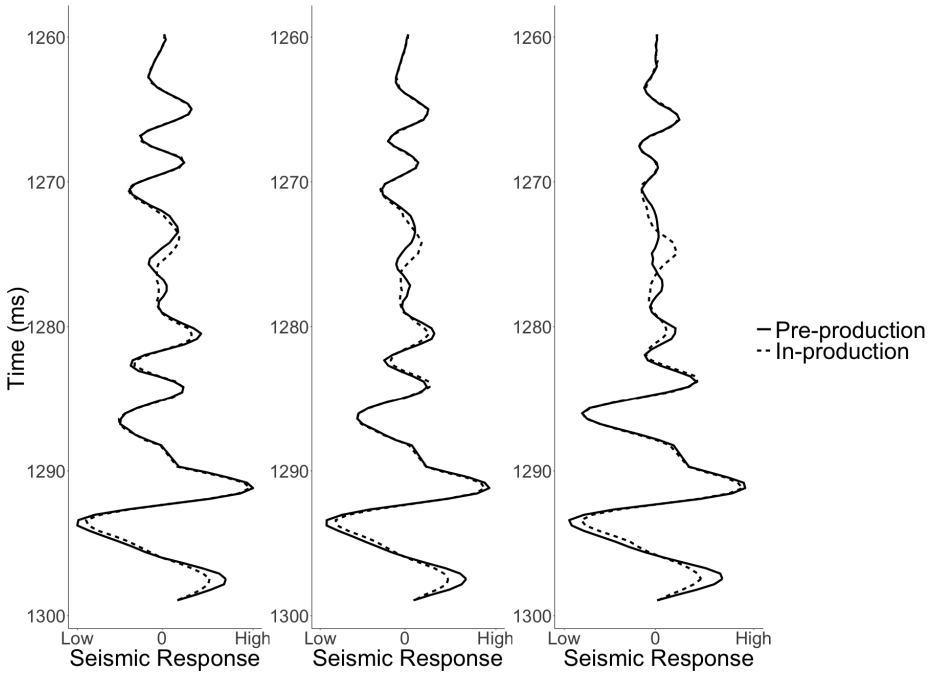

Fig. 2. Time-lapse seismic AVO data. The seismic AVO data pre-production (solid lines) and in-production (dashed lines). The left, middle, and right displays correspond to the 8° stack, 24° stack, and 40° stack, respectively.

multiple facies, we recommend to adopt a lithology-dependent rock physics model. The effect of water saturation is assumed to be constant in time; hence, the coefficients contained in both $\mathbf{B}^0$ and $\mathbf{B}^1$ can be estimated at the pre-production stage.

In Table I, the numerical values of the estimated coefficients and standard deviations associated with the Gauss-linear rock physics likelihood model are displayed. The estimated cross-covariance between the elastic properties are $\hat{\xi}_{z_p z_s}$, $\hat{\xi}_{z_p \rho}$, and $\hat{\xi}_{z_s \rho}$, with corresponding correlations 0.737, 0.156, and 0.400.

From Table I, we note that porosity is assigned more explanatory power than water saturation. In Fig. 3, the regression models are displayed. Each display in the figure represents a projection into a bivariate domain. Any remaining variability in the elastic properties is probably due to variations in mineral fractions and rock texture. The dominant explanatory power of porosity is notably reflected in the distance between the lines, which is relatively small in the left column when s_w^0 is fixed. This is particularly evident in the model for

TABLE I

ESTIMATED PARAMETERS IN THE ROCK PHYSICS LIKELIHOOD MODEL. THE ESTIMATED INTERCEPT $\hat{\alpha}$, SLOPE OF POROSITY $\hat{\beta}_\phi$, AND SLOPE OF WATER SATURATION $\hat{\beta}_{s_w^0}$, ARE DISPLAYED TOGETHER WITH THE ESTIMATED STANDARD DEVIATION $\hat{\sigma}$ FOR EACH REGRESSION MODEL IN THE TOP TABLE. EACH ROW OF THE TABLE CONTAINS THE PARAMETERS ASSOCIATED WITH THE MODEL FOR THE ELASTIC PROPERTY SPECIFIED IN THE LEFTMOST COLUMN. THE ESTIMATED CROSS-COVARIANCE BETWEEN THE ELASTIC PROPERTIES, $\hat{\xi}_{z_p z_s}$, $\hat{\xi}_{z_p \rho}$, AND $\hat{\xi}_{z_s \rho}$, ARE SHOWN IN THE LOWER TABLE

	$\hat{\alpha}$	$\hat{\beta}_\phi$	$\hat{\beta}_{s_w^0}$	$\hat{\sigma}$
$\log(z_p)$	9.123	-1.201	0.081	0.068
$\log(z_s)$	8.563	-1.050	0.013	0.074
$\log(\rho)$	0.967	-0.832	0.044	0.025

$\hat{\xi}_{z_p z_s}$	$\hat{\xi}_{z_p \rho}$	$\hat{\xi}_{z_s \rho}$
$3.74 \cdot 10^{-3}$	$2.68 \cdot 10^{-4}$	$7.51 \cdot 10^{-4}$

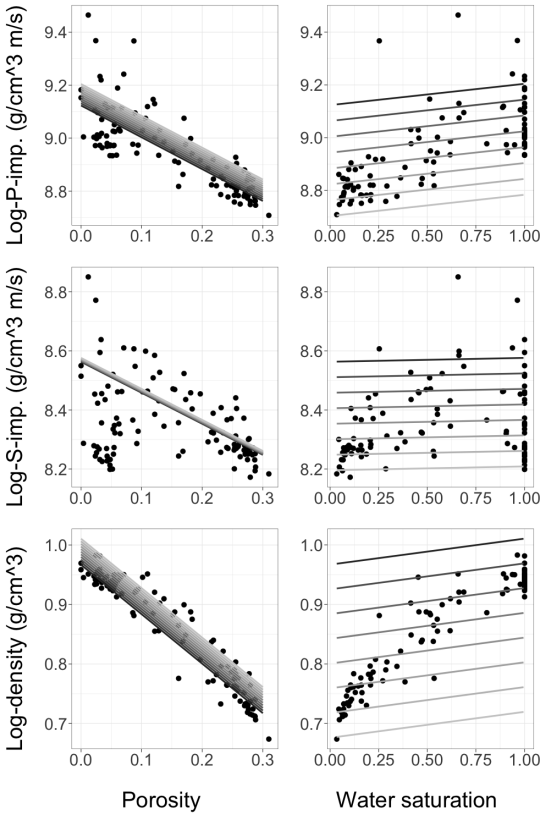

Fig. 3. (Left Column) Estimated relationship between the elastic properties and porosity, with water saturation fixed to a value in $[0, 1]$ with step size 0.1. (Right Column) Estimated relationship between the elastic properties and water saturation, with porosity fixed to a value in $[0.1, 0.25]$ with step size 0.05. The color of the lines gradually transitions from black to white, corresponding to minimum and maximum values, respectively. The true elastic properties are indicated by points.

log-S-impedance. Indeed, the shear modulus is not affected by the fluid, therefore the fluid effect on S-impedance only depends on the density.

B. Prior Model

The parameters used in the prior model are listed in Table II. The prior model $p(\mathbf{s}_w^1)$ is assumed to be the same as $p(\mathbf{s}_w^0)$,

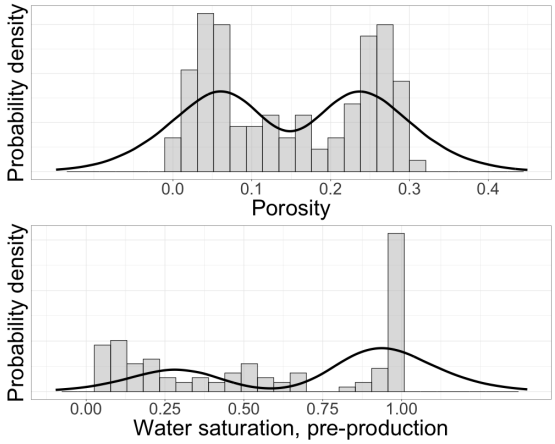

Fig. 4. Histograms of the true reservoir properties pre-production together with marginal prior models (solid lines). (Top) Porosity. (Bottom) Water saturation pre-production.

TABLE II

PARAMETER VALUES USED IN THE PRIOR S-GRF. THE PARAMETERS ASSOCIATED WITH THE BASIS GRF MODEL ARE SHOWN IN THE TOP; THE EXPECTATION LEVELS $(\mu_{\tilde{\phi}}, \mu_{\tilde{s}_w^0}, \mu_{\tilde{s}_w^1})$ IN THE LEFTMOST BLOCK, THE VARIANCE LEVELS $(\sigma^2_{\tilde{\phi}}, \sigma^2_{\tilde{s}_w^0}, \sigma^2_{\tilde{s}_w^1})$ IN THE MIDDLE BLOCK, AND THE CORRELATIONS λ_k, $k = 1, 2, 3$ BETWEEN THE VARIABLES IN THE RIGHTMOST BLOCK. THE PARAMETERS ASSOCIATED WITH THE AUXILIARY GRF ARE SHOWN IN THE MIDDLE; THE MARGINAL SELECTION SETS A_k IN THE LEFT BLOCK, AND THE CORRELATIONS WITH THE BASIS GRF γ_k, $k = 1, 2, 3$ IN THE RIGHT BLOCK. THE RANGE PARAMETER α_r ASSOCIATED WITH THE SPATIAL CORRELATION STRUCTURE IS LISTED IN THE BOTTOM

$\mu_{\tilde{\phi}}$	0.149
$\mu_{\tilde{s}_w^0}$	0.662
$\mu_{\tilde{s}_w^1}$	0.662

$\sigma^2_{\tilde{\phi}}$	0.010
$\sigma^2_{\tilde{s}_w^0}$	0.070
$\sigma^2_{\tilde{s}_w^1}$	0.070

λ_1	-0.8
λ_2	-0.4
λ_3	0.4

A_1	$(-\infty, -0.5] \cup [0.5, \infty)$	γ_1	0.90
A_2	$(-\infty, -1.2] \cup [0.7, \infty)$	γ_2	0.90
A_3	$(-\infty, -1.2] \cup [0.7, \infty)$	γ_3	0.90

α_r	0.8

coinciding with the conservative assumption of time stationary water saturation. The intervariable correlations between the basis GRF $\tilde{\mathbf{s}}_w^1$ and the basis GRFs $\tilde{\boldsymbol{\phi}}$ and $\tilde{\mathbf{s}}_w^0$ are assigned to be -0.4 and 0.4, respectively.

The marginal prior models, together with spatial histograms of the pre-production truth, are displayed in Fig. 4. The two modes in the marginal prior for porosity are not as clearly separated as the modes in the marginal prior for the water saturations. The prior model should cover the truth, but also be conservative in the sense of having larger variability. Note that the prior model supports values outside the physical range $[0, 1]$.

One realization from the prior model, together with 90% HPrD (highest prior density) intervals, are displayed in Fig. 5. The HPrD intervals reflect the marginal prior distributions, and since they are constant along the study interval, also the stationarity of the RF. As expected, the HPrD intervals indicate bimodality in the marginal prior for the water saturations, but not in the marginal prior for porosity. From the figure, we see

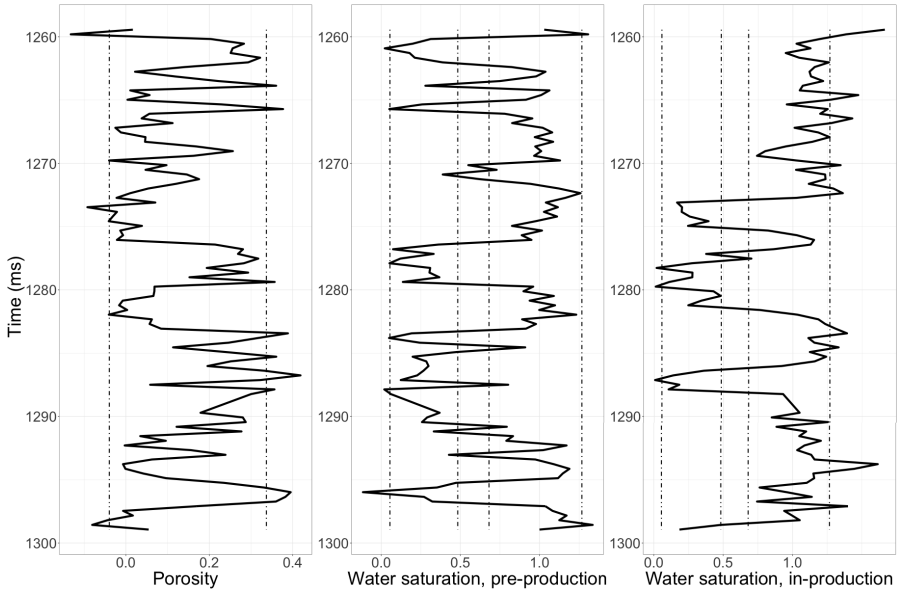

Fig. 5. One realization from the prior model. The realization (solid lines) is displayed with 90% HPrD intervals (dot-dashed lines). (Left) Porosity. (Middle) Water saturation pre-production. (Right) Water saturation in-production.

that the realization of each reservoir property is marginally informed by the prior model, and that they contain abrupt mode transitions along the entire study interval. The prior model is marginally informative, but noninformative with respect to the location of mode transitions. The abrupt mode transitions are more evident in the realization of the water saturations than in porosity. The realization of porosity is below zero at some locations, while the realization of the water saturations frequently exceed one, but is rarely below zero.

C. Results

The predicted reservoir properties with associated prediction intervals are shown in Fig. 6. The true reservoir properties are displayed for validation. The predicted reservoir properties and their 90% HPD prediction intervals are [0, 1]-truncated. Note that the truncation of the predictions almost only occurs for predictions of water saturations exceeding 1, and rarely for predictions of porosity below 0. The results for porosity appear to be very reliable; the MMAP prediction greatly coincides with the truth, and the HPD prediction interval appears to be reasonable. Note that the prediction interval does not reflect bimodality in the marginal posterior distributions, but appears as relatively wide at some locations since the posterior modes are not sufficiently distinct. The results for the water saturations also appear to be very reliable. The abrupt mode transitions seen in the true water saturations are reproduced in the predictions, and the prediction intervals appear to be reasonable. The pre-production prediction appears to be very accurate, except for slightly overpredicting between 1270 and 1280 ms. The in-production prediction also appears highly reliable, but the first mode transition from the top seen in the pre-production result is not reproduced. Bimodality in the marginal posteriors is reflected in the prediction intervals at several locations, especially near the locations of mode transitions. The prediction intervals reflect bimodality at the pre-production stage less often than at the in-production stage, indicating more uncertainty in the latter. This is as expected since the prior model is assigned based on the pre-production truth.

TABLE III
EMPIRICAL CORRELATION BETWEEN THE MMAP PREDICTIONS AND THE TRUTH, AND EMPIRICAL COVERAGE OF THE 90% HPD PREDICTION INTERVALS

	Empirical correlation	Empirical coverage
$\hat{\boldsymbol{\phi}}$	0.816	0.876
$\hat{\mathbf{s}}_w^0$	0.828	0.876
$\hat{\mathbf{s}}_w^1$	0.763	0.904

Note the marked difference in the marginal posterior distributions reflected in the HPD prediction intervals in Fig. 6 compared to the marginal prior distributions seen in Fig. 5. This difference clearly illustrates the effect of conditioning the model on the time-lapse seismic AVO data.

The correlation between the predictions and the truth and the empirical coverage of the 90% HPD prediction intervals are listed in Table III. By construction, the expected empirical correlation between a realization from the prior model and the truth is zero. The empirical correlation between the MMAP predictions and the truth are notably higher, reflecting the influence of the seismic data on the model. As expected, the correlation associated with porosity and pre-production water saturation is higher than the correlation associated with the in-production water saturation. Moreover, the empirical coverage greatly coincides with the specified coverage, indicating that the prior model reflects the variability in the truth.

V. 2-D APPLICATION: CO_2 SEQUESTRATION

We apply the proposed seismic inversion methodology to a time-lapse geophysical monitoring study for a project in

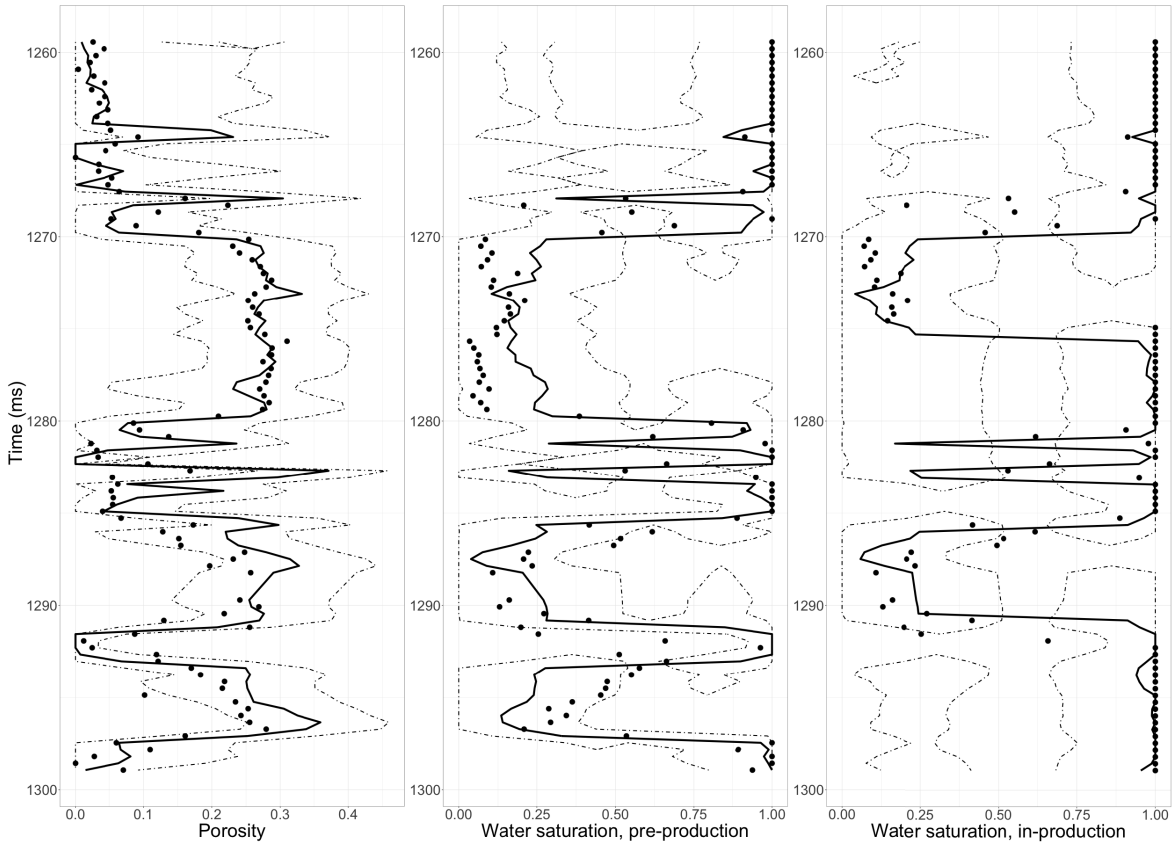

Fig. 6. Inversion result. The MMAP predictions (solid lines) are displayed with 90% HPD prediction intervals (dot-dashed lines) and the truth (dots). (Left) Porosity. (Middle) Water saturation pre-production. (Right) Water saturation in-production.

the Johansen formation, a potential CO_2 storage unit, located offshore Norway, underneath the Troll field ([38] and [39]). An overview of the geology for the Johansen formation and the overlying sealing layers is given in [38]. The rock formation is a sandstone unit with relatively high average porosity and permeability. Porosity and permeability are assumed to be constant in time. Simulations of CO_2 injection and migration using two-phase fluid flow modeling are presented in [39]. The initial porosity and the fluid saturation predicted by fluid flow simulations to years 10 and 100 are referred to as the truth. This truth is used to generate synthetic time-lapse seismic AVO data. Density is computed as a linear combination of the density of the solid and fluid phases weighted by the pore volume. Velocities are computed using the soft sand model that integrates the Hertz-Mindlin equations, Hashin-Shtrikman lower bounds, and Gassmann's equations [40]. Uncorrelated Gaussian noise is added to the synthetic data assuming an SNR of 5. We assume to be in a setting where the true reservoir and elastic properties are only known in year 10; hence, a model fitting must be based on these. However, the simulated saturation profile in year 100 will be used to validate the inversion result.

The 2-D section is gridded by 41 vertical traces, each of which consists of 10 and 11 trace-unique locations for the seismic grid and reservoir grid, respectively. The reservoir grid $\mathcal{G}_r$ therefore consists of $n_r = 451$ locations, regularly spaced horizontally, and with trace-unique vertical gridding. The seismic grid $\mathcal{G}_d$ consists of $n_d = 410$ locations with similar structure. Visualizing the data and results on the reservoir and seismic grids is challenging because of the irregularity caused by the trace-unique vertical gridding. The calculations are therefore performed on the uneven grid, but we linearly interpolate to a regular grid to enable visualization. Note that this may smooth the appearance of the presented data and results to some degree.

The time-lapse seismic AVO data used in the study is presented in Figs. 7 and 8, representing seismic AVO data from the CO_2 reservoir after 10 and 100 years of production, respectively. The seismic data consist of $n_\theta = 3$ angle stacks, which are displayed row-wise in the figures. In Fig. 7, the signal stands out as relatively strong in the middle traces, which coincides with the location of the CO_2. The signal appears weaker to the right of the CO_2 region than to the left of it, which is a consequence of the geometry of the high porosity region. The seismic signal shown in Fig. 8 is similar to the signal from year 10, but the middle region of relatively high seismic response is now bigger. This is expected because the CO_2 region has expanded.

A. Likelihood Model

Since the seismic data are synthetically generated from the elastic properties, we have full knowledge of the seismic model $[\mathbf{d}|\mathbf{m}] = \mathbf{WADm} + \mathbf{e}_{d|m}$; hence, only the parameters of the rock physics model $[\mathbf{m}|\mathbf{r}] = \mathbf{Br} + \mathbf{e}_{m|r}$ must be estimated.

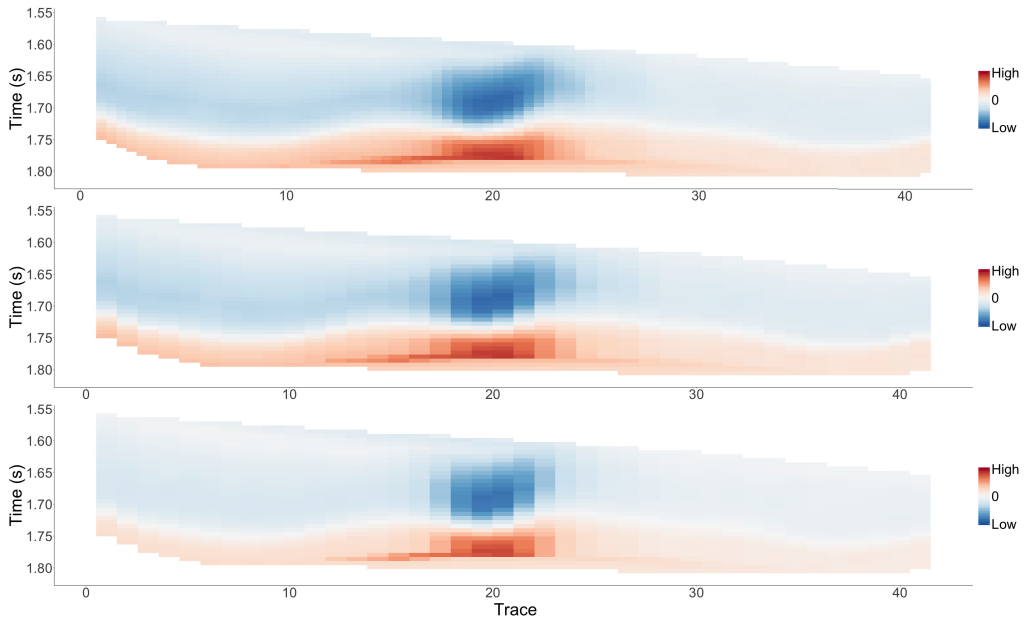

Fig. 7. Seismic AVO data from year 10. The top, middle, and bottom displays correspond to the 8° stack, 24° stack, and 40° stack, respectively.

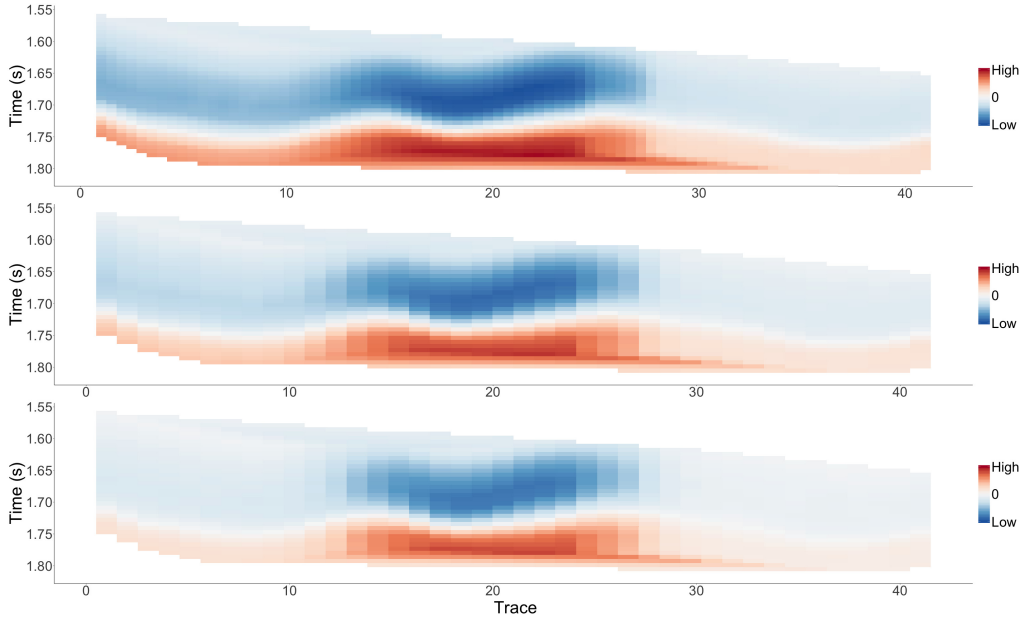

Fig. 8. Seismic AVO data from year 100. The top, middle, and bottom displays correspond to the 8° stack, 24° stack, and 40° stack, respectively.

This entails estimating the coefficients contained in $\mathbf{B}$ and the entries in the covariance matrix $\mathbf{\Sigma}_{m|r}$. We assume the effect of water saturation to be constant in time, and therefore estimate the coefficients contained in $\mathbf{B}^0$ and $\mathbf{B}^1$ from the true reservoir and elastic properties in year 10.

In Table IV, the numerical values of the estimated coefficients and standard deviations associated with the Gauss-linear rock physics likelihood model are displayed. The estimated cross-covariance between the elastic properties are $\hat{\xi}_{z_p z_s}$, $\hat{\xi}_{z_p \rho}$, and $\hat{\xi}_{z_s \rho}$, with corresponding correlations 0.806, 0.061, and -0.116. Since the two latter correlations are low, we assume them to be zero; hence, independence between the involved elastic properties. Note that porosity is assigned more explanatory power than water saturation, and this is reflected in Fig. 9, which displays the regression models.

B. Prior Model

The parameter values used in the prior model are listed in Table V. The prior model $p(\mathbf{s}_w^1)$ is assumed to be the same as $p(\mathbf{s}_w^0)$, coinciding with the conservative assumption of time stationary water saturation. We also assume that the pdf of the basis GRF $p(\tilde{\mathbf{r}})$ can be expressed

$$p(\tilde{\mathbf{r}}) = p(\tilde{\boldsymbol{\phi}})\, p(\tilde{\mathbf{s}}_w^0)\, p(\tilde{\mathbf{s}}_w^1). \tag{24}$$

This assumption of independence between the reservoir properties, particularly between the water saturations, may not

TABLE IV

ESTIMATED PARAMETERS IN THE ROCK PHYSICS LIKELIHOOD MODEL. THE ESTIMATED INTERCEPT $\hat{\alpha}$, SLOPE OF POROSITY $\hat{\beta}_\phi$, AND SLOPE OF WATER SATURATION $\hat{\beta}_{s_w^0}$, ARE DISPLAYED TOGETHER WITH THE ESTIMATED STANDARD DEVIATION $\hat{\sigma}$ FOR EACH REGRESSION MODEL IN THE TOP TABLE. EACH ROW OF THE TABLE CONTAINS THE PARAMETERS ASSOCIATED WITH THE MODEL FOR THE ELASTIC PROPERTY SPECIFIED IN THE LEFTMOST COLUMN. THE ESTIMATED CROSS-COVARIANCE BETWEEN THE ELASTIC PROPERTIES, $\hat{\xi}_{z_p z_s}$, $\hat{\xi}_{z_p \rho}$, AND $\hat{\xi}_{z_s \rho}$, ARE SHOWN IN THE LOWER TABLE

	$\hat{\alpha}$	$\hat{\beta}_\phi$	$\hat{\beta}_{s_w^0}$	$\hat{\sigma}$
$\log(z_p)$	9.144	-2.798	0.241	0.005
$\log(z_s)$	8.821	-3.470	0.056	0.005
$\log(\rho)$	0.884	-0.676	0.090	0.001

$\hat{\xi}_{z_p z_s}$	$\hat{\xi}_{z_p \rho}$	$\hat{\xi}_{z_s \rho}$
$2.32 \cdot 10^{-5}$	0	0

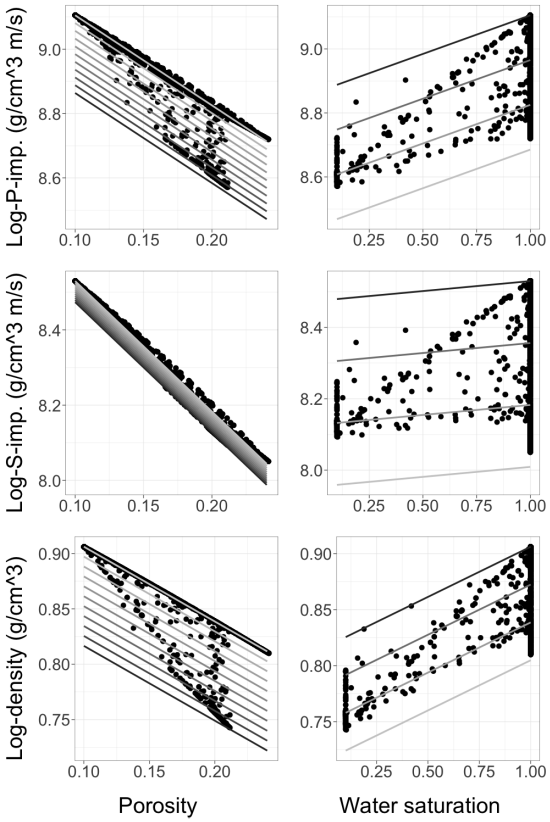

Fig. 9. (Left Column) Estimated relationship between the elastic properties and porosity, with water saturation fixed to a value in $[0, 1]$ with step size 0.1. (Right Column) Estimated relationship between the elastic properties and water saturation, with porosity fixed to a value in $[0.1, 0.25]$ with step size 0.05. The color of the lines gradually transition from black to white, corresponding to minimum and maximum values, respectively. The true elastic properties are indicated by points.

be realistic. However, specifying a correlation is problematic since it does not capture the causal relationship between the water saturations, and it appears to be highly trace dependent. With no correlations specified, the methodology relies more heavily on the seismic data than it otherwise would.

The marginal prior models, together with spatial histograms of the truth in year 10, are displayed in Fig. 10. The two

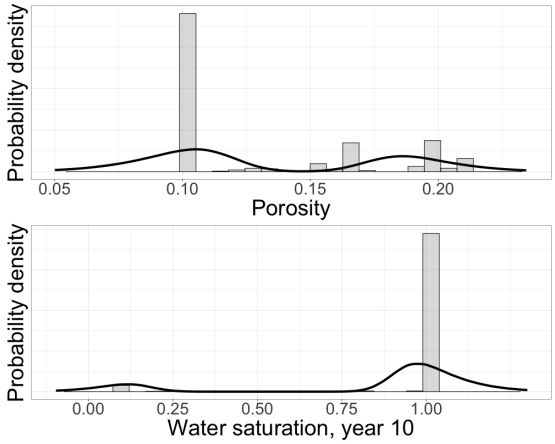

Fig. 10. Histograms of the true reservoir properties in year 10 together with marginal prior models. (Top) Porosity. (Bottom) Water saturation.

TABLE V

PARAMETER VALUES USED IN THE PRIOR S-GRF. THE PARAMETERS ASSOCIATED WITH THE BASIS GRF MODEL ARE SHOWN IN THE TOP; THE EXPECTATION LEVELS $(\mu_{\tilde{\phi}}, \mu_{\tilde{s}_w^0}, \mu_{\tilde{s}_w^1})$ IN THE LEFTMOST BLOCK, THE VARIANCE LEVELS $(\sigma^2_{\tilde{\phi}}, \sigma^2_{\tilde{s}_w^0}, \sigma^2_{\tilde{s}_w^1})$ IN THE MIDDLE BLOCK, AND THE CORRELATIONS λ_k, $k = 1, 2, 3$ BETWEEN THE VARIABLES IN THE RIGHTMOST BLOCK. THE PARAMETERS ASSOCIATED WITH THE AUXILIARY GRF ARE SHOWN IN THE MIDDLE; THE MARGINAL SELECTION SETS A_k IN THE LEFT BLOCK, AND THE CORRELATIONS WITH THE BASIS GRF γ_k, $k = 1, 2, 3$ IN THE RIGHT BLOCK. THE RANGE PARAMETER α_r ASSOCIATED WITH THE SPATIAL CORRELATION STRUCTURE IS LISTED IN THE BOTTOM

$\mu_{\tilde{\phi}}$	0.141
$\mu_{\tilde{s}_w^0}$	0.619
$\mu_{\tilde{s}_w^1}$	0.619

$\sigma^2_{\tilde{\phi}}$	0.001
$\sigma^2_{\tilde{s}_w^0}$	0.054
$\sigma^2_{\tilde{s}_w^1}$	0.054

λ_1	0
λ_2	0
λ_3	0

A_1	$(-\infty, -0.7] \cup [1, \infty)$	γ_1	0.95
A_2	$(-\infty, -2] \cup [1.3, \infty)$	γ_2	0.97
A_3	$(-\infty, -2] \cup [1.3, \infty)$	γ_3	0.97

α_r	0.005

modes in the marginal priors are clearly separated. The prior model should cover the truth, but also be conservative in the sense of having larger variability. However, since the data are very distinctly grouped, it is challenging to assign a prior model with representative variability. This is particularly challenging for the water saturations since the data is almost binary. Moreover, the histogram of the true porosity may have three modes; hence, a bimodal prior model may not be fully representative.

One realization from the prior model is displayed in Fig. 11. We see that the realization of each reservoir property is similar in that they all contain abrupt mode transitions seemingly without pattern over the entire 2-D section. They are different in that the porosity is mostly low-valued with many high-valued speckles, while the water saturations are mostly high-valued with few low-valued speckles. The prior realization with 90% HPrD intervals through trace 22 is displayed in Fig. 12. The realization abruptly transitions between modes along the trace, and bimodality in the prior model is clearly

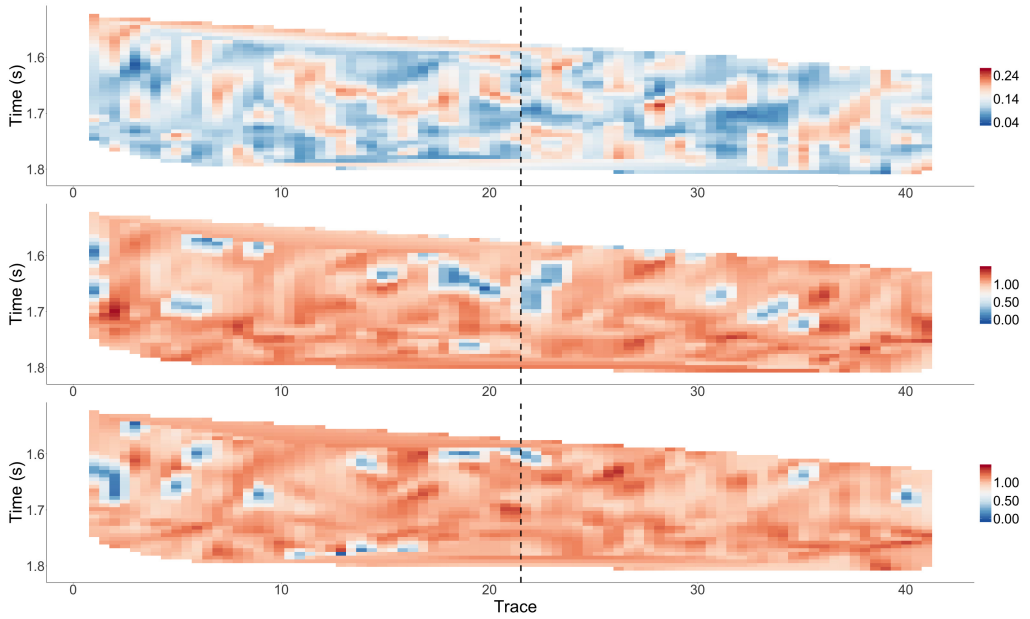

Fig. 11. One realization from the prior model. (Top) Porosity. (Middle) Water saturation in year 10. (Bottom) Water saturation in year 100. The dashed line through trace 22 indicates the vertical profile we consider closer.

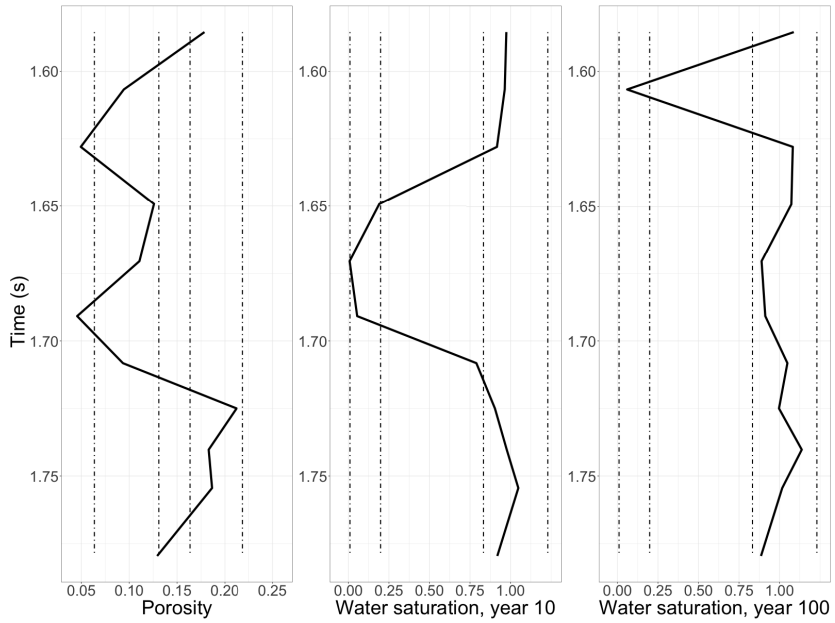

Fig. 12. Prior realization through trace 22. The realization (solid lines) is displayed with 90% HPrD intervals (dot-dashed lines). (Left) Porosity. (Middle) Water saturation in year 10. (Right) Water saturation in year 100.

reflected in the HPrD interval of each reservoir property. Since the prior model is stationary, the HPrD intervals are constant along the trace.

C. Results

The predicted porosity, water saturation in year 10, and water saturation in year 100 are shown in Figs. 13–15, respectively. For comparison, the true porosity and water saturations are also displayed. The prediction of porosity appears to be reliable. The shape of the predicted region with comparatively higher porosity is very similar to the truth, with the exception of the lowest of the two thin subregions to the right. This region is particularly difficult to predict because it is very thin and contains porosity values in the mid-range that are hard to differentiate from the lower values. The predicted porosity values are overall in good agreement with the truth. The predictions of the water saturations appear to be highly reliable. The high and low values are correctly located, and the shape of the regions with comparatively low water saturations is very similar to the truth.

Since the prediction plots are interpolated, and therefore somewhat smoothed, we present the predictions with

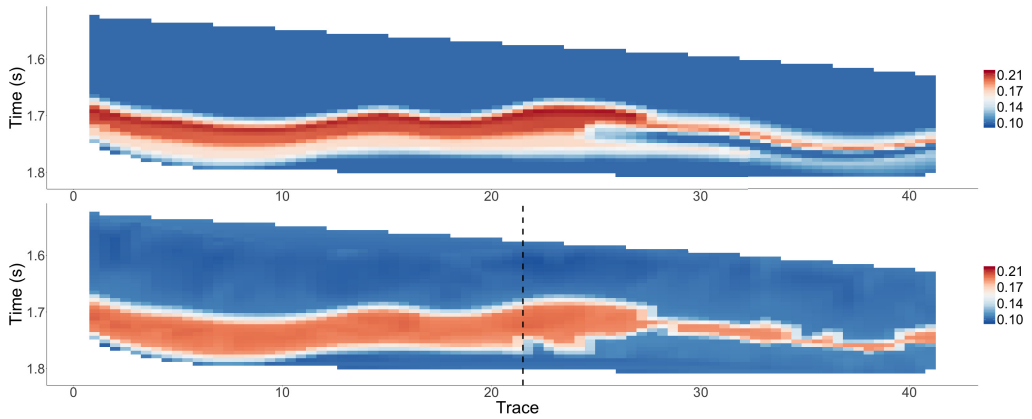

Fig. 13. Inversion result for porosity. (Top) Truth. (Bottom) MMAP. The dashed line through trace 22 in the MMAP indicates the vertical profile we consider closer.

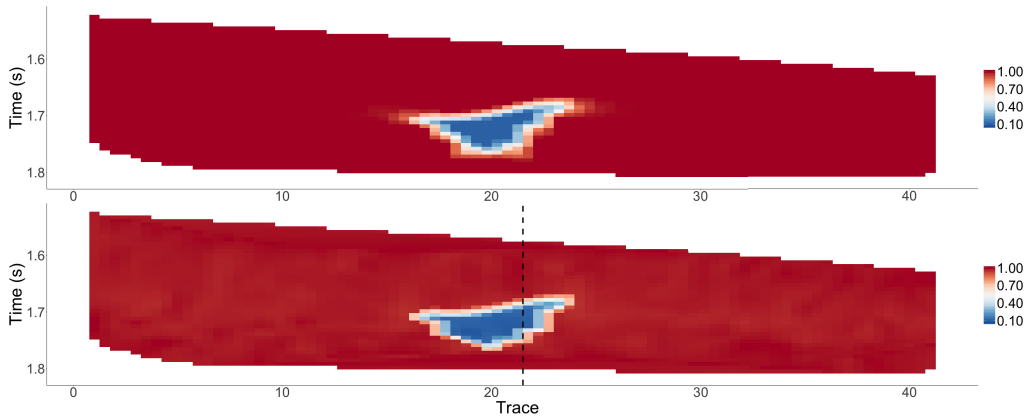

Fig. 14. Inversion result for water saturation in year 10. (Top) Truth. (Bottom) MMAP. The dashed line through trace 22 in the MMAP indicates the vertical profile we consider closer.

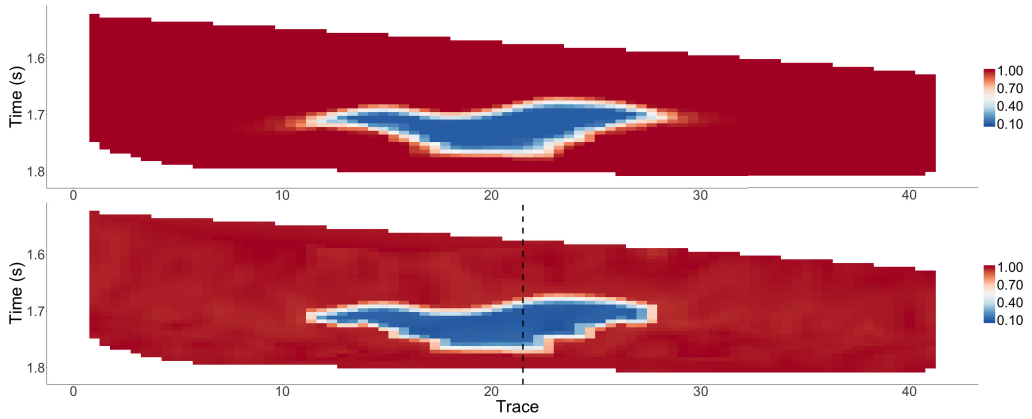

Fig. 15. Inversion result for water saturation in year 100. (Top) Truth. (Bottom) MMAP. The dashed line through trace 22 in the MMAP indicates the vertical profile we consider closer.

associated 90% HPD prediction intervals together with the truth in original grid format along the vertical profile through trace 22 in Fig. 16. Note that the true CO_2 region is relatively small in year 10, but covers the entire porous layer in year 100. Also note that the bimodality of the posterior distribution is clearly reflected in the prediction intervals. The prediction of porosity appears to be reliable; the predicted porosities deviate from the truth only to a small extent and the posterior distribution appears unimodal except for near the mode transitions. The two water saturations also appear to be reliably predicted. The predicted values match the truth well in both cases, but the high-to-low mode transition in the predicted water saturation in year 10 is a bit too low. Note that the predictions are rarely truncated, and when they are, the effect is not big since the true MMAP is just barely larger than 1. The posterior distribution of water saturation in year 10 appears to

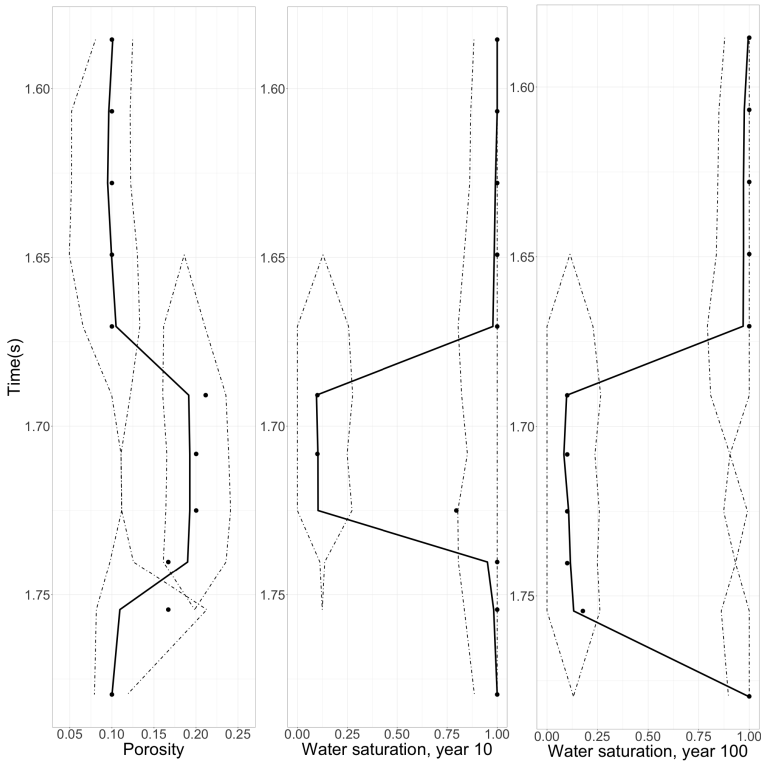

Fig. 16. Inversion result through trace 22. The MMAP predictions (solid lines) are displayed with 90% HPD prediction intervals (dot-dashed lines) and the truth (dots). (Left) Porosity. (Middle) Water saturation in year 10. (Right) Water saturation in year 100.

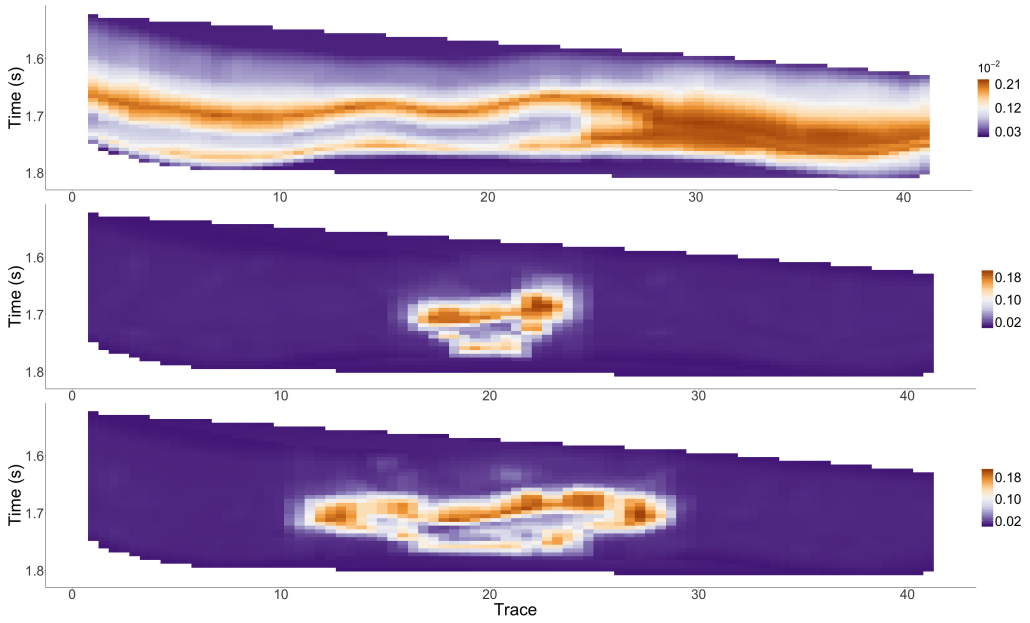

Fig. 17. Variance of posterior samples. (Top) Porosity. (Middle) Water saturation in year 10. (Bottom) Water saturation in year 100.

have a high valued mode throughout the entire profile. Here, the CO_2 region is small, causing the posterior to be somewhat uncertain. However, the probability of the high valued mode does seem to shrink in this region. The posterior distribution of water saturation in year 100 displays much unimodality, but bimodality can be seen near the locations of the mode transitions and to a small extent in the middle of the CO_2 region.

The prediction variances are presented in Fig. 17. As expected, the variances are high near the borders separating the two qualitatively different regions for each reservoir property. Note also the large variance in the porosity predictions to the right, where the two thin subregions are located.

The correlation between the predictions and the truth, and the empirical coverage of the 90% HPD prediction intervals

TABLE VI
EMPIRICAL CORRELATION BETWEEN THE MMAP PREDICTIONS AND THE TRUTH, AND EMPIRICAL COVERAGE OF THE 90% HPD PREDICTION INTERVALS

	Empirical correlation	Empirical coverage
$\hat{\boldsymbol{\phi}}$	0.884	0.967
$\hat{\mathbf{s}}_w^0$	0.961	0.991
$\hat{\mathbf{s}}_w^1$	0.979	0.978

are displayed in Table VI. As expected, the correlation associated with each reservoir property is high, but higher for the water saturations than for porosity. The relatively low correlation associated with porosity is most likely a result of the bimodal prior model not being fully representative of the possibly trimodal characteristics of porosity. The computed coverages are somewhat higher than the specified 90%, which indicates that the variability in the prior model may be too high. This is as expected, since the reservoir properties exhibit quite distinct levels which are challenging to model.

The methodology is validated on a 2-D problem, but it can be extended to 3-D studies in a trace by trace inversion setting. Each trace is indeed inverted independently and the continuity of the results depends on the continuity of the input seismic data. The computational cost of the inversion increases linearly with the number of traces.

VI. CONCLUSION

The time-lapse seismic AVO inversion problem is approached in a Bayesian framework where the likelihood model is Gauss-linear and the prior model is an S-GRF. The likelihood model captures the joint effect of the reservoir properties on the seismic data at both time points. The prior model is chosen due to its ability to represent multimodality and to reproduce abrupt spatial mode transitions, seen in the reservoir properties. The model makes it possible to do joint seismic inversion for the two time points, and the inversion result is represented by the posterior model. The methodology is demonstrated on two realistic synthetic cases; on predicting the changes along a 1-D profile of an oil reservoir induced by oil production, and on predicting the expansion of a CO_2 region in a 2-D section of a subsurface potential CO_2 storage unit caused by injection of CO_2.

The inversion methodology reproduces the abrupt mode transitions seen in the true reservoir properties and provides reliable inversion results in both cases. In the 2-D case, the reservoir properties are distinctly multimodal and appear to correlate in a complex way. These characteristics are challenging to model, and specifying a prior model with representative variability is particularly hard. The 1-D case is not as problematic because the reservoir properties are not as distinctly multimodal and since the correlation has to be specified along one trace only. Moreover, the inversion methodology is capable of predicting relatively thin layers of locally extreme values. This is particularly evident in the 1-D case. However, the mid-valued thin lower subregion in the true porosity in the 2-D case is not reproduced in the prediction. This is likely caused by the prior model of porosity not being fully representative, and the absence of lateral correlation in the prior model may be a contributing factor. The prior model can be extended to honor geological layering better by introduction of lateral correlation. This is computationally more expensive because it requires trace conditioning, but may improve resolution in the 2-D case. Overall, the results are very encouraging, indicating that the proposed model formulation and statistical assumptions are particularly suited for fluid flow monitoring problems.

ACKNOWLEDGMENT

This research is part of the Uncertainty in Reservoir Evaluation (URE) activity at the Norwegian University of Science and Technology (NTNU). The authors acknowledge SINTEF for providing the MATLAB Reservoir Simulation Toolbox, and the R-packages *MASS* and *akima*. Lastly, the authors would like to thank the School of Energy Resources and the Nielson Energy Fellowship for the support.

REFERENCES

[1] R. Calvert, *Insights and Methods for 4D Reservoir Monitoring and Characterization*. Tulsa, OK, USA: Society of Exploration Geophysicists and European Association of Geoscientists & Engineers, 2005.
[2] T. L. Davis, M. Landrø, and M. Wilson, *Geophysics and Geosequestration*. Cambridge, U.K.: Cambridge Univ. Press, 2019.
[3] G. Mavko, T. Mukerji, and J. Dvorkin, *The Rock Physics Handbook*. Cambridge, U.K.: Cambridge Univ. Press, 2009.
[4] K. Aki and P. G. Richards, *Quantitative Seismology: Theory Methods*. San Francisco, CA, USA: Freeman, 1980.
[5] A. Tarantola, *Inverse Problem Theory Methods for Model Parameter Estimation*. Philadelphia, PA, USA: SIAM, 2005.
[6] P. Doyen, *Seismic Reservoir Characterization: An Earth Modelling Perspective*, vol. 2. Houten, The Netherlands: EAGE, 2007.
[7] D. E. Lumley, "Time-lapse seismic reservoir monitoring," *Geophysics*, vol. 66, no. 1, pp. 50–53, 2001.
[8] M. Landrø, "Discrimination between pressure and fluid saturation changes from time-lapse seismic data," *Geophysics*, vol. 66, no. 3, pp. 836–844, 2001.
[9] M. Landrø, H. H. Veire, K. Duffaut, and N. Najjar, "Discrimination between pressure and fluid saturation changes from marine multicomponent time-lapse seismic data," *Geophysics*, vol. 68, no. 5, pp. 1592–1599, Sep. 2003.
[10] H. H. Veire, H. G. Borgos, and M. Landrø, "Stochastic inversion of pressure and saturation changes from time-lapse AVO data," *Geophysics*, vol. 71, no. 5, pp. C81–C92, Sep. 2006.
[11] S. Grude, M. Landrø, and B. Osdal, "Time-lapse pressure–saturation discrimination for CO_2 storage at the Snøhvit field," *Int. J. Greenhouse Gas Control*, vol. 19, pp. 369–378, Nov. 2013.
[12] T. Bhakta and M. Landrø, "Estimation of pressure-saturation changes for unconsolidated reservoir rocks with highVP/VSratio," *Geophysics*, vol. 79, no. 5, pp. M35–M54, Sep. 2014.
[13] M. Meadows, "Time-lapse seismic modeling and inversion of CO_2 saturation for storage and enhanced oil recovery," *Lead. Edge*, vol. 27, no. 4, pp. 506–516, 2008.
[14] M. Trani, R. Arts, O. Leeuwenburgh, and J. Brouwer, "Estimation of changes in saturation and pressure from 4D seismic AVO and time-shift analysis," *Geophysics*, vol. 76, no. 2, pp. C1–C17, Mar. 2011.
[15] X. Lang and D. Grana, "Rock physics modelling and inversion for saturation-pressure changes in time-lapse seismic studies," *Geophys. Prospecting*, vol. 67, no. 7, pp. 1912–1928, Sep. 2019.
[16] A. Buland and Y. E. Ouair, "Bayesian time-lapse inversion," *Geophysics*, vol. 71, no. 3, pp. R43–R48, May 2006.
[17] K. Rimstad, P. Avseth, and H. Omre, "Hierarchical Bayesian lithology/fluid prediction: A North sea case study," *Geophysics*, vol. 77, no. 2, pp. B69–B85, Mar. 2012.
[18] D. Grana and T. Mukerji, "Bayesian inversion of time-lapse seismic data for the estimation of static reservoir properties and dynamic property changes," *Geophys. Prospecting*, vol. 63, no. 3, pp. 637–655, May 2015.
[19] S. Yuan, S. Wang, M. Ma, Y. Ji, and L. Deng, "Sparse Bayesian learning-based time-variant deconvolution," *IEEE Trans. Geosci. Remote Sens.*, vol. 55, no. 11, pp. 6182–6194, Nov. 2017.

[20] F. L. Bordignon, L. P. de Figueiredo, L. Azevedo, A. Soares, M. Roisenberg, and G. S. Neto, "Hybrid global stochastic and Bayesian linearized acoustic seismic inversion methodology," *IEEE Trans. Geosci. Remote Sens.*, vol. 55, no. 8, pp. 4457–4464, Aug. 2017.
[21] Q. Guo, H. Zhang, H. Cao, W. Xiao, and F. Han, "Hybrid seismic inversion based on multi-order anisotropic Markov random field," *IEEE Trans. Geosci. Remote Sens.*, vol. 58, no. 1, pp. 407–420, Jan. 2020.
[22] K. B. Zoeppritz, "Vllb. On reflection and transmission of seismic waves by surfaces of discontinuity," in *Nachrichten von der Königlichen Gesellschaft der Wissenschaften zu Göttingen, Mathematischphysikalische Klasse*. 1919, pp. 66–84.
[23] A. Buland and H. Omre, "Bayesian linearized AVO inversion," *Geophysics*, vol. 68, no. 1, pp. 185–198, Jan. 2003.
[24] D. Grana, T. Fjeldstad, and H. Omre, "Bayesian Gaussian mixture linear inversion for geophysical inverse problems," *Math. Geosci.*, vol. 49, no. 4, pp. 493–515, May 2017.
[25] D. W. Oldenburg, "An introduction to linear inverse theory," *IEEE Trans. Geosci. Remote Sens.*, vol. GRS-22, no. 6, pp. 665–674, Nov. 1984.
[26] A. Buland, O. Kolbjørnsen, and H. Omre, "Rapid spatially coupled AVO inversion in the Fourier domain," *Geophysics*, vol. 68, no. 3, pp. 824–836, May 2003.
[27] K. Mosegaard and A. Tarantola, "Monte Carlo sampling of solutions to inverse problems," *J. Geophys. Res., Solid Earth*, vol. 100, no. B7, pp. 12431–12447, Jul. 1995.
[28] L. P. de Figueiredo, D. Grana, M. Roisenberg, and B. B. Rodrigues, "Multimodal Markov chain Monte Carlo method for nonlinear petrophysical seismic inversion," *Geophysics*, vol. 84, no. 5, pp. M1–M13, Sep. 2019.
[29] V. Hasselblad, "Estimation of parameters for a mixture of normal distributions," *Technometrics*, vol. 8, no. 3, pp. 431–444, Aug. 1966.
[30] G. Matheron, H. Beucher, C. de Fouquet, and A. Galli, "Conditional simulation of the geometry of fluvio-deltaic reservoirs," in *Proc. Annu. Tech. Conf. Exhib. (SPE)*, Dallas, TX, USA, Sep. 1987, pp. 591–599.
[31] H. Omre and K. Rimstad, "Bayesian spatial inversion and conjugate selection Gaussian prior models," 2018, *arXiv:1812.01882*. [Online]. Available: http://arxiv.org/abs/1812.01882
[32] D. V. Lindberg and H. Omre, "Blind categorical deconvolution in two-level hidden Markov models," *IEEE Trans. Geosci. Remote Sens.*, vol. 52, no. 11, pp. 7435–7447, Nov. 2014.
[33] D. V. Lindberg and H. Omre, "Inference of the transition matrix in convolved hidden Markov models and the generalized Baum–Welch algorithm," *IEEE Trans. Geosci. Remote Sens.*, vol. 53, no. 12, pp. 6443–6456, Dec. 2015.
[34] T. Fjeldstad and H. Omre, "Bayesian inversion of convolved hidden Markov models with applications in reservoir prediction," *IEEE Trans. Geosci. Remote Sens.*, vol. 58, no. 3, pp. 1957–1968, Mar. 2020.
[35] R. B. Arellano-Valle and A. Azzalini, "On the unification of families of skew-normal distributions," *Scandin. J. Statist.*, vol. 33, no. 3, pp. 561–574, Sep. 2006.
[36] O. B. Forberg, H. Omre, and Ø. Kjøsnes, "Bayesian seismic AVO inversion for reservoir variables with bimodal spatial histograms," *Geophysics*, 2021.
[37] D. Grana and E. D. Rossa, "Probabilistic petrophysical-properties estimation integrating statistical rock physics with seismic inversion," *Geophysics*, vol. 75, no. 3, pp. O21–O37, May 2010.
[38] G. T. Eigestad, H. K. Dahle, B. Hellevang, F. Riis, W. T. Johansen, and E. Øian, "Geological modeling and simulation of CO_2 injection in the Johansen formation," *Comput. Geosci.*, vol. 13, no. 4, p. 435, 2009.
[39] P. E. S. Bergmo, A.-A. Grimstad, and E. Lindeberg, "Simultaneous CO_2 injection and water production to optimise aquifer storage capacity," *Int. J. Greenhouse Gas Control*, vol. 5, no. 3, pp. 555–564, May 2011.
[40] J. Dvorkin, M. A. Gutierrez, and D. Grana, *Seismic Reflections Rock Properties*. Cambridge, U.K.: Cambridge Univ. Press, 2014.

Ole Bernhard Forberg received the M.Sc. degree in industrial mathematics from the Norwegian University of Science and Technology (NTNU), Trondheim, Norway, in 2017, where he is pursuing the Ph.D. degree in statistics with the Department of Mathematical Sciences.

He joined the "Uncertainty in Reservoir Evaluation" (URE) research initiative with NTNU in 2017. His main research interests are Bayesian inversion and computationally intensive statistical methods, with a particular interest in spatio-temporal statistics, seismic inversion, and selection Gaussian random fields.

Dario Grana received the M.Sc. degree in applied mathematics from the University of Milan-Bicocca, Milan, Italy, in 2006, and the Ph.D. degree in geophysics from Stanford University, Stanford, CA, USA, in 2013.

He worked four years at Eni Exploration and Production in Milan. He joined the University of Wyoming, Laramie, WY, USA, in 2013, where he is an Associate Professor with the Department of Geology and Geophysics. He has coauthored the book *Seismic Reflections of Rock Properties*, published by Cambridge University Press in 2014. His main research interests are rock physics, seismic reservoir characterization, geostatistics, data-assimilation, and inverse problems for subsurface modeling.

Dr. Grana was a recipient of the 2017 EAGE Van Weelden Award, the 2016 SEG Karcher Award, the 2015 Best Paper Award in Mathematical Geosciences, and the 2014 Eni Award with Gary Mavko, Tapan Mukerji, and Jack Dvorkin for "pioneering innovations in theoretical and practical rock physics for seismic reservoir characterization".

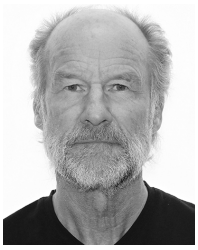

Henning Omre received the M.Sc. degree in statistics from the Norwegian University of Science and Technology (NTNU), Trondheim, Norway, in 1975, and the Ph.D. degree in geostatistics from Stanford University, Stanford, CA, USA, in 1985.

He worked with the Norwegian Computing Center, Oslo, Norway, from 1976 to 1992. He joined NTNU as a Professor in 1992. From 1994 to 2019, he was the Head of the research initiative "Uncertainty in Reservoir Evaluation" (URE). He is a Professor of statistics with the Department of Mathematical Sciences, NTNU. His main research interests are spatio-temporal statistics and Bayesian inversion.

Dr. Omre was a recipient of the 1996 Statoil Research Award, the 2011 EAGE Alfred Wegener Award for "outstanding contributions in geostatistics for reservoir applications," and the 2019 Sverdrup Award for "contributions to the field of statistics in Norway."